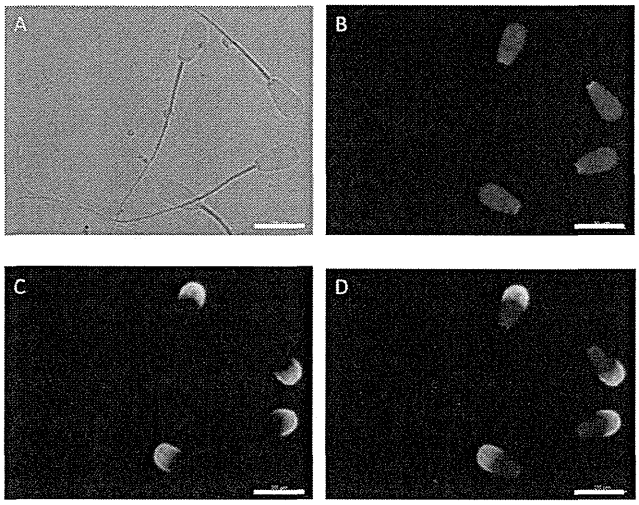

Figure 1 | Bull epididymal sperm nuclei and acrosomes stained with 4′,6′-diamino-2′-phenylindole (DAPI) and fluorescein isothiocyanate (FITC-PNA). A. Phase-contrast, B. DAPI-stained, C. FITC-PNA stained, and D. DAPI + FITC-PNA- stained images. Scale bar, 20 μm; magnification, 1000×.

Alterations of micro-constituents in irradiated testes. Figures 3A to 3D: 3,4,5, and 6 show phase maps indicating the concentrations of the micro-constituents carbon (C), molybdenum (Mo), potassium (K), and Cs, respectively. Colour imaging can rapidly and effectively facilitate the overall analysis of the composite structure: decreasing levels of metal distribution are indicated from red to black. In the control image, the C imaging result was shown as intermediate (light green) in the seminiferous tubules; however, Mo levels were low (blue) and K was not detected in germ cells (Figure 3A: 3, 4, and 6). Interestingly, in the testis of bull 1, C imaging result indicated high to intermediate levels (red and light green); however, it showed low levels of Mo (dark blue; Figure 3B: 3, 4). In contrast, similar expression patterns of C, Mo, and K were observed in the testes of both bull 2 and the control (Figure 3C: 3, 4, and 5). A comparison of foetal and control colour map imaging results revealed that C and Mo levels were higher expression patterns in the foetal testis (Figure 3D: 3, 4). However, Cs was not detected in any of the bull testes, including the foetal sample (Figure 3A–D: 5).

Since testicular Cs was not detectable by EPMA, we determined Cs concentration by ICP-MS in the control testis. We found that the mole ratio of radioactive Cs to stable Cs was at the order of 10^{-5} (Table 4).

Discussion

The risk of external and internal radiation exposure to health is of great concern worldwide. Analysis of 14 species of birds common to Fukushima and Chernobyl revealed a negative effect of radiation on abundance, and the relationship was more strongly negative in Fukushima than in Chernobyl[15]. The effect of radiation on farm animals in the evacuation zone following the FNPP accident provides information about the health risks of livestock and can also be extrapolated to humans. Cattle are assumed to have received high doses of irradiation in radioactively contaminated environments, because they consume large amounts of vegetation and drinking water, resulting in accumulation of radionuclides in their bodies[16] as well as external exposure from terrestrial radionuclides. This study was designed to provide insight into the biological response of bull testes to different doses of radiation following the FNPP accident.

Although various types of radionuclides were released into the environment, radioactive substances of major concern now are

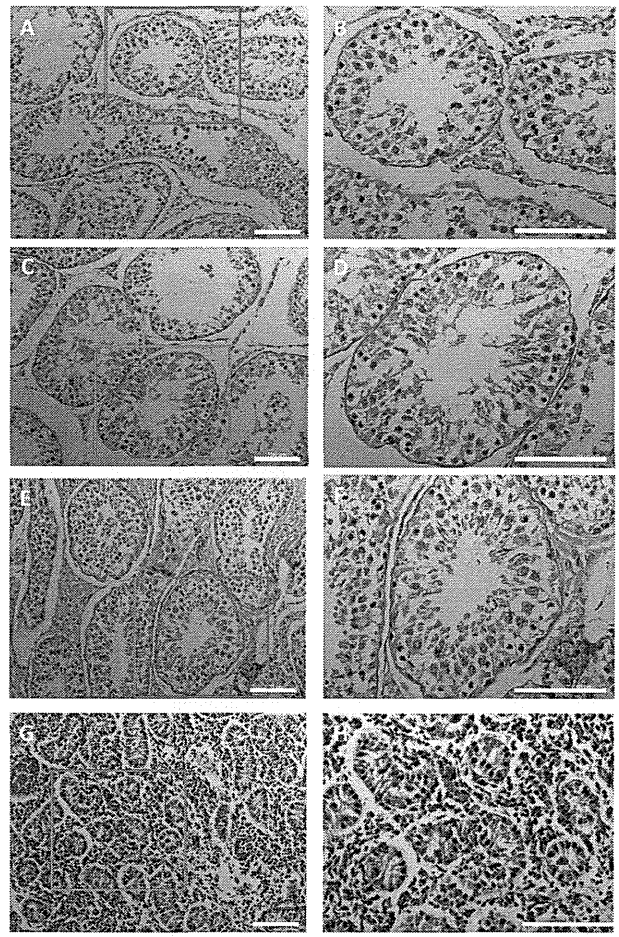

Figure 2 | Histological sections of the seminiferous tubules of bull testes. A, B. Images of control bull testis. C–F. Images of bull exposed to radiation. G, H. Images of seminiferous tubules from foetal testes. Scale bar, 100 μm.

^{134}Cs and ^{137}Cs because of their relatively long half-life. The internal dose varies in a more complex manner than the external dose depending on a number of factors such as soil-to-plant ratio, the distance to the nearest forest, dietary habits, water, air, and body burden[17]. These factors make it difficult to estimate chronic irradiation of wildlife under natural conditions[18]. We recently revealed that the levels of ^{134}Cs and ^{137}Cs were the same in all the organs examined and that concentration of radioactive Cs in each organ was significantly correlated with that in PB in an organ-specific manner; moreover, radionuclide deposition was strongly affected by the environment where the cattle were caught[13]. We calculated effective internal exposure from the concentration of radioactive caesium in organs and effective external dose from that in soil obtained in our study[13]. Since the testis is a relatively radiosensitive organ, we considered that radiation exposure would lead to changes in the morphology or the function of this organ. Activity concentration of radioactive caesium was 13- to 18-fold higher in the testis than in PB for liquid. Radioactivity concentration of caesium in the testis was about more than half of that in the skeletal muscle and the level was the same as in other organs. The ratio of external exposure to internal exposure in the testis of bull 1 was 1.6- to 2.5-fold and in that of bull 2 was 0.20- to 0.38-fold. This indicates that contribution of external exposure to total exposure is not negligible compared to internal exposure. Organ-specific concentration of radiocaesium in the foetus, compared with bull 1 and bull 2, of this study showed that

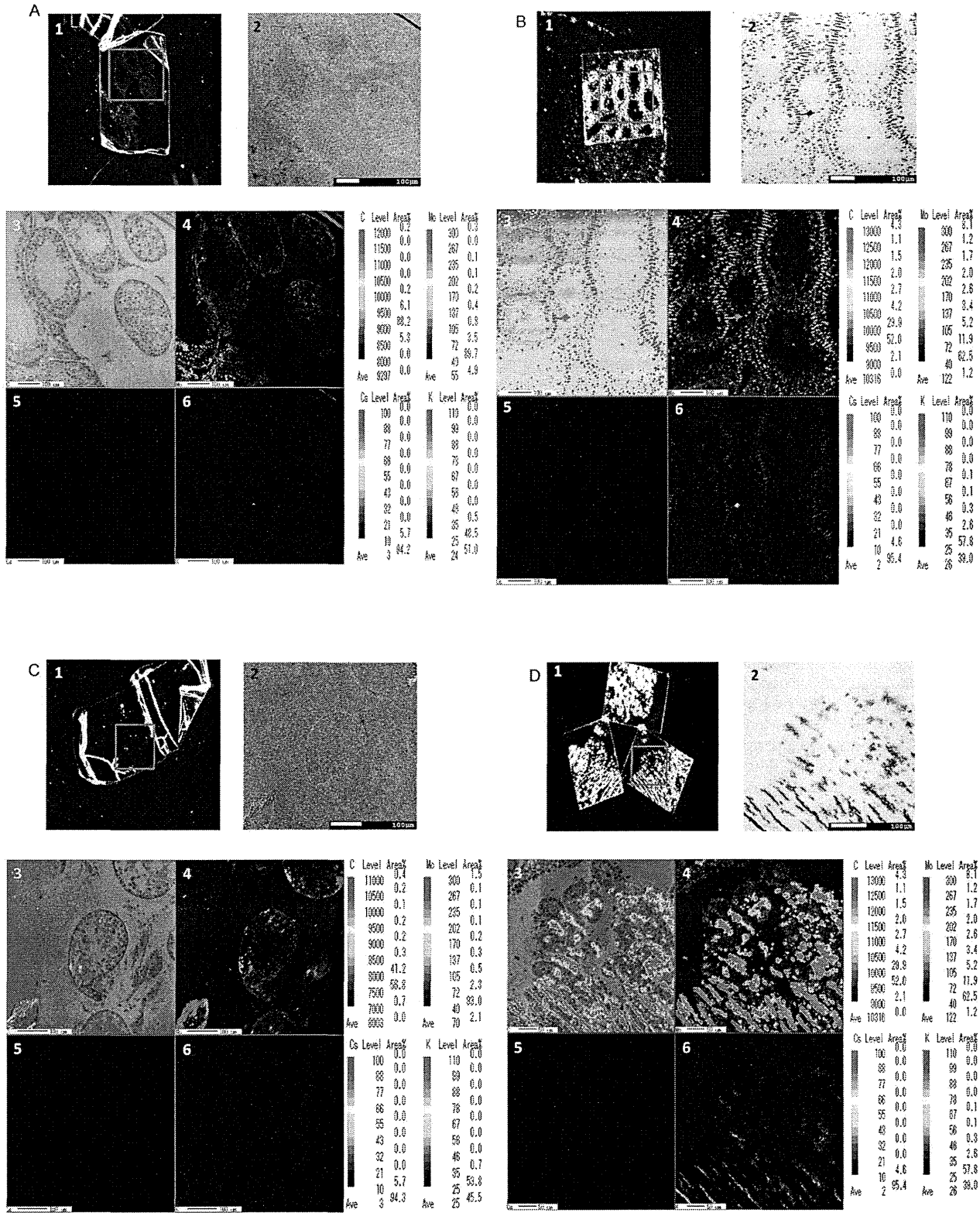

Figure 3 | EPMA analysis of bull testis. A. Control, B. Bull No. 1, C. Bull No. 2, D. Foetus. 1. Stereo-microscopy images of bull testis. 2. Composite backscattered electron microscopy images. 3. Secondary electron colour map image of C (carbon) regions. 4. Corresponding distribution of Mo (molybdenum) obtained for the same section. 5. X-ray colour-coded phase map of Cs (caesium). 6. Corresponding X-ray profiles for K (potassium). Scale bar, 100 μm (50 μm for Figure 3D: 3–6).

Table 4 | Testicular concentration of ^{133}Cs, ^{134}Cs and ^{137}Cs

	^{134}Cs		^{137}Cs		^{133}Cs		(^{134}Cs + ^{137}Cs)/^{133}Cs
	mg/kg ($\times 10^{-10}$)	mol/kg ($\times 10^{-13}$)	mg/kg ($\times 10^{-9}$)	mol/kg ($\times 10^{-12}$)	mg/kg ($\times 10^{-4}$)	mol/kg ($\times 10^{-7}$)	($\times 10^{-5}$ fold)
No. 1	40.6	0.30	66.6	0.49	ND*	ND*	1.6
No. 2	134.0	1.00	206.6	1.51	ND*	ND*	5.1
Foetus	39.0	0.29	62.5	0.46	ND*	ND*	1.5
Control	ND*	ND*	ND*	ND*	41.7	0.31	ND*

Concentrations of radioactive Cs were calculated from the values in Table 2 using specific activity of ^{134}Cs (4.8×10^{-10} Bq/mg) and of ^{137}Cs (3.2×10^{-9} Bq/mg), respectively.
*ND: Not determined.

radiocaesium is transferred to the foetus from its mother through the placenta and the deposition is organ dependent.

Spermatogenesis is a complex process of male germ cell proliferation and maturation from spermatogonia to spermatozoa in the seminiferous tubules of the testis. Spermatogonia are especially sensitive to irradiation; doses as low as 0.1 Gy are known to cause damage to these cells[5]. Carefully controlled small animal experiments have indicated that effects of low-dose radiation (LDR) and high-dose radiation (HDR) on the testis are different. Exposure to HDR has an inhibitory effect on genomic and cytological changes. However, exposure to LDR has a stimulatory effect on the metabolism, antioxidant capacity, proliferation, and maturation of male mouse germ cells. This phenomenon is termed hormesis[19]. Taki et al. analysed alterations in gene expression profiles in mouse testes continuously irradiated with HDR or LDR for 485 days. They reported that expression of genes categorized as 'DNA metabolism', 'response to DNA damage', and 'DNA replication' in the gene ontology are inversely correlated with dose rate to the testis[20]. Some studies have suggested that exposure to LDR leads to adaption to the subsequent exposure to HDR, known as adaptive responses[24]. Male mouse foetuses exposed to radiation at 5–6 weeks of pregnancy are at an increased risk of developing testicular cancer in mice[21]. The present study revealed that chronic exposure to radiation even from conception onwards did not affect foetal germ cell morphology.

EPMA is a powerful tool for detecting trace chemical elements in both single cells and tissues by measuring the characteristic X-ray spectra to specific elements within samples through the use of an accelerated electron beam[22]. However, we could not detect Cs by EPMA because the detection limit of EPMA is 100 ppm (0.1 g/kg)[23]. Therefore, we measured stable ^{133}Cs in the testes of non-radio-contaminated control by inductively coupled plasma-mass spectrometer (ICP-MS) as a representative concentration of total Cs in the testis. The ratio of radioactive Cs to total Cs in the testis was calculated by (^{134}Cs + ^{137}Cs)/^{133}Cs of control. The ratio was at 10^{-5} order, indicating that chemical toxicity of radioactive Cs is negligible. Considering that the bulls in this study were exposed to various radionuclides as well as ^{134}Cs and ^{137}Cs, we suggest that spermatogenesis occurred normally following long-term exposure to the levels of radioactive substances in the evacuation zone of the FNPP accident.

In conclusion, no adverse radiation-induced effects were observed in bull testes following chronic exposure to 3.6–4.6 mGy for bull 1 and 6.9–11.4 mGy for bull 2 for up to 10 months. These data improve our understanding of the effect of radiation on bull reproductive organs exposed to long-term radiation, and emphasize the importance of assessing the effect of nuclear accidents on reproduction. Dubrova et al. reported that the frequency of germ-line mini-satellite mutations among children born to parents who resided in constantly polluted areas (>250 kBq/m^2) after the Chernobyl accident is about twice as high as in controls[25]. The air dose rate in the evacuation zone was the highest on March 15, 2011 and has been continuously declining mainly because the decay of ^{134}Cs. The air dose rate now, 2 years after the FNPP accident, is three quarters of the highest levels[26]. Furthermore, marginal areas of the evacuation zone have been decontaminated. Therefore, it is now impossible to investigate more animals from the different annual dose field to cover the range up to the deterministic threshold for gonads. In order to develop a system of protection against radiation, the long-term impact of radiation on large animals within the FNPP evacuation zone needs to be continuously investigated. The study to compare whole genome sequences among bulls in the evacuation zone of FNPP, foetuses obtained by fertilization using sperm from bulls in the evacuation zone, and control bulls is underway in our laboratory. The negative results observed here may not represent the whole picture of radiation effects. Further investigation on the effect of ionizing radiation on spermatogenesis should be extended to more animals.

Methods

Ethics. This study is one of the national projects associated with the Great East Japan Earthquake and has been entirely endorsed and supported by the Japanese government through the Ministry of Education, Culture, Sports, Science and Technology, Japan. The Japanese government ordered Fukushima prefecture to euthanize cattle in the evacuation zone on 12 May 2011 to prevent radio-contaminated beef products from entering the human food chain. We obtained organs and testes from the euthanized bull collected by the combined unit of veterinary doctors belonging to the Livestock Hygiene Service Centre (LHSC) of Fukushima prefecture and those belonging to the Ministry of Agriculture, Forestry and Fisheries, Japan. These veterinarians euthanized the bulls by using the following method according to the Regulation for Animal Experiments and Related Activities at Tohoku University (Regulation No 122). The ear tag of the cattle identified the owner of each bull, and informed consent from the owner was obtained by the veterinary doctors of Fukushima prefecture. Control testes were obtained at a castration operation for fattening of a feeder. The procedure of euthanasia was entirely carried out by the veterinary doctors of LHSC. The Ethics Committee of Animal Experiments, Tohoku University approved this study.

Animals. We collected testes from 12 euthanized Japanese black beef bulls and 3 foetuses between 29 August 2011 and 24 January 2012. Those were 4 castrated and 2 calve and testes from 4 bulls were used for sperm collection. One foetus was female and another was too small. Therefore, we could analyse the testis samples from 2 euthanized bulls and 1 male foetus. Testes from bull 1 (date of birth, 21 October 2010) and a foetus (body length approximately 80 cm, approximately 8-month gestation) were collected in Kawauchi village located 15 km southwest of FNPP on 27 September 2011: the air dose rate was 0.5 μSv/h, radioactivity concentration in the soil was ^{134}Cs 230 kBq/m^2 and ^{137}Cs 240 kBq/m^2, and the time elapsed since the major release of radioactive caesium was 196 days. Testes from bull 2 (more than 1 year old) were collected in Naraha town located 17 km south of FNPP on 24 January 2012: the air dose rate was 2 μSv/h, radioactivity concentration in the soil was ^{134}Cs 100 kBq/m^2 and ^{137}Cs 110 kBq/m^2, and the time elapsed since the FNPP accident was 315 days. Testes from control Japanese black beef (11 months old) were collected from a non-radio-contaminated site in Miyagi prefecture on 7 March 2012.

Calculation method of internal and external dose rates. Dose rates of internal and external exposure to ^{134}Cs and ^{137}Cs were calculated according to the method of dosimetry assumption described in ICRP Publication 108[27].

We adopted several assumptions for the estimation of internal dose rate. Average radioactivity concentration of the total body was calculated by the mean of radioactivity concentrations of organs determined. Legs were excluded from the object of evaluation. From the body length and the depth and width of the chest, we calculated the conversion coefficient of dose rate.

External dose rate was calculated based on the concentrations of ^{134}Cs and ^{137}Cs in soil, assuming certain distance between soil surface and the body mentioned above. The external exposures of ^{134}Cs and ^{137}Cs during certain duration were calculated as

follows:

$$\int_0^T 24CA\left(\frac{1}{2}\right)^{\frac{t}{T_{1/2}}}dt = \frac{24}{ln2}CAT_{1/2}\left\{\left(\frac{1}{2}\right)^{\frac{T}{T_{1/2}}}-1\right\}$$

C; coefficient (μGy/h/(Bq/m^2)), 2.04 × 10^{-6} for ^{134}Cs and 7.3 × 10^{-7} for ^{137}Cs.
A; radioactivity concentration in the soil (kBq/m^2), 230 for ^{134}Cs and 240 for ^{137}C for bull 1, and 100 for ^{134}Cs and 110 for ^{137}C for bull 2 as of March 15, 2011.
$T_{1/2}$; half-life (days), 754 for ^{134}Cs and 11,016 for ^{137}Cs.
T; period from March 15 to the day of capture (days), 196 for bull 1 and 315 for bull 2.

Measurements of radioactivity. Tissue radioactivity was determined by gamma-ray spectrometry using 3 HPGe detectors (ORTEC, USA). The relative efficiencies of the detectors were 30%, 20%, and 15% with a resolution at the 1.33 MeV line of 1.9 keV, 1.9 keV, and 1.8 keV, respectively. The time taken for the measurements varied from 3,600 s to 200,000 s, depending on the radioactivity of the samples. The detection efficiency was determined by measuring mixed sources of Eu-152 and ^{137}Cs. An aliquot (200 μl) of the mixed source was diluted with appropriate amounts of water, and superabsorbent polymer was added to the mixture to obtain a gel standard source, which was used for mock samples that imitated organ tissues. Several different gel sources were prepared to cover a weight range of 0.5–130 g. Aqueous solutions of Eu-152 and ^{137}Cs were used to determine the detection efficiency of liquid samples (e.g. blood cells, serum, and whole blood).

Blood samples. Although the blood samples collected were immediately placed into ice packs, on-site sample manipulation resulted in high variability. Most potassium is located within cells and caesium competes with potassium for active and passive membrane transport. In preliminary experiments using 6 bulls, the haematocrit was fairly constant (approximately 55%); however, the blood cell-to-plasma ratio for ^{137}Cs varied from 1.5 to 5.2. We found that ^{137}C radioactivity for liquid in whole blood reasonably reflected organ-specific radioactivity, and therefore adopted blood ^{137}Cs radioactivity for liquid as a standard in this study.

Evaluation of epididymal sperm nucleus and acrosome integrity. The nucleus and acrosome of fresh epididymal sperm of bull were stained with 4′,6′-diamino-2′-phenylindole (DAPI; Invitrogen) and fluorescein isothiocyanate (FITC-PNA; Sigma), according to the procedure described by Yamashiro et al[28].

Morphological assessment of testis cells. Testes were fixed in 10% paraformaldehyde, embedded in paraffin, and stained with haematoxylin and eosin (HE) according to standard protocols. Briefly, fixed testes were dehydrated in a series of different concentrations of alcohol, made transparent with dimethylbenzene, embedded in paraffin, and cut into 5-μm-thick sections, before staining.

Electron probe X-ray microanalysis (EPMA). Chemical trace analysis of Cs (caesium), C (carbon), K (potassium), and Mo (molybdenum) in testicular structures was performed by JOEL (Tokyo, Japan) using a JXA-8230 SuperProbe Electron Probe Microanalyzer (JOEL) equipped for X-ray spectrometry and specially adapted for the examination of ultrathin sections. Specimens were loaded using a silicon wafer and focused by an electronic beam of 0.3 μm diameter. For analysis, the voltage of the electron microscope was set to 15 kV and the rate of the electron beam was 1 μA. The sections were viewed as secondary electron images, and mapping was performed using the chemical elemental mode.

Measurement of tissue ^{133}Cs level. Tissue sample was digested with 2 ml of HNO_3 (Wako) at 105°C for 6–18 h and dried. The processed samples were dissolved completely with 2% HNO_3 to a final volume of 20 ml. An inductively coupled plasma-mass spectrometer (ICP-MS, ELAN DRC-e; PerkinElmer SCIEX, Concord, ON, Canada) was used for measurement of Cs.

1. Mettler, F. A. & Voelz, G. L. Major radiation exposure – What to expect and how to respond. *Engl. J. Med.* **346**, 1554–1561 (2002).
2. Kinoshita, N. *et al.* Assessment of individual radionuclide distributions from the Fukushima nuclear accident covering central-east Japan. *Proc. Natl. Acad. Sci.* **108**, 19526–19529 (2011).
3. Zheng, J. *et al.* Isotopic evidence of plutonium release into the environment from the Fukushima DNPP accident. *Sci. Rep.* **2**, 304 (2012).
4. Chute, J. P. To survive radiation injury, remember your aPCs. *Nat. Med.* **18**, 1013–1014 (2012).
5. Otala, M. *et al.* Protection from Radiation-Induced Male Germ Cell Loss by Sphingosine-1-Phosphate. *Biol. Reprod.* **70**, 759–767 (2004).
6. Liu, G. *et al.* Effect of low-level radiation on the death of male germ cells. *Radiat. Res.* **165**, 379–389 (2006).
7. Pierce, D. A., Shimizu, Y., Preston, D. L., Vaeth, M. & Mabuchi, K. Studies of the mortality of atomic bomb survivors. Report 12, part 1. Cancer: 1950–1990. *Radiat. Res.* **146**, 1–27 (1996).
8. Katayama, H. *et al.* Reassessment of the cancer mortality risk among Hiroshima atomic-bomb survivors using a new dosimetry system, ABS2000D, compared with ABS93D. *J. Radiat. Res.* **43**, 53–63 (2002).
9. Yablokv, A. V., Nesterenko, V. B. & Nesterenko, A. V. Chernobyl: Consequences of the Catastrophe for People and the Environment. *Annals of the New York academy of sciences Volume* **1181**, 1–327 (2009).
10. Storer, J. B., Mitchell, T. J. & Fry, R. J. M. Extrapolation of the relative risk of radiogenic neoplasms across mouse strains and to man. *Radiat. Res.* **114**, 331–353 (1988).
11. Shiragai, A. *et al.* Estimation of the absorbed dose to mice in prolonged irradiation by low-dose rate gamma-rays from 137Cs sources. *Radioisotopes.* **46**, 904–911 (1997).
12. EPA. Cancer risk coefficients for environmental exposure to radionuclides. Federal Guidance Report No. 13, EPA 402–R–99–001, Office of Radiation and Indoor Air (Environmental Protection Agency, Washington, DC (1999).
13. Fukuda, T. *et al.* Distribution of artificial radionuclides in the abandoned cattle in the evacuation zone of the Fukushima Daiichi Nuclear Power Plant. *PloS One* **8**, e54312 (2013).
14. Calabrese, E. Improving the scientific foundations for estimating health risks from the Fukushima incident. *Proc. Natl. Acad. Sci.* **108**, 19447–19448 (2011).
15. Moller, A. P. *et al.* Abundance of birds in Fukushima as judged from Chernobyl. *Environ Pollut.* **164**, 36–39 (2012).
16. International Atomic Energy Agency (IAEA). Environmental consequences of the Chernobyl accident and their remediation: Twenty Years of experience. Report of the Chernobyl forum expert group 'Environment', Vienna, 2006.
17. Thornberg, C. *et al.* External and internal irradiation of a rural Bryansk (Russia) population from 1990 to 2000, following high deposition of radioactive caesium from the Chernobyl accident. *Radiat. Environ. Biophys.* **44**, 97–106 (2005).
18. Vives, I. *et al.* Inter-comparison of population models for the calculation of radiation dose effects on wildlife. *Radiat. Environ. Biophys.* **51**, 399–410 (2005).
19. Liu, G. *et al.* Apoptotic cell death induced by low-dose radiation in male germ cells: hormesis and adaptation. *Crit. Rev. Toxicol.* **37**, 587–605 (2007).
20. Taki, K. *et al.* Microarray analysis of differentially expressed genes in the kidneys and testes of mice after long-term irradiation with low-dose-rate γ-rays. *J. Radiat. Res.* **50**, 241–252 (2009).
21. Shetty, G., Comish, P. B., Weng, C. C., Matin, A. & Meistrich, M. L. Fetal radiation exposure induces testicular cancer in genetically susceptible mice. *PLoS One* **7**, e32064 (2012).
22. Pogorelov, A., Budantsev, G., Yu, A. & Pogorelova, V. N. Quantitative electron probe microanalysis of acetylcholinesterase activity in rat brain sections. *J. Histochem. Cytochem.* **41**, 1795–1800 (1993).
23. Reed, SJB. Quantitative trace analysis by wavelength dispersive EPMA. *Mikrochim. Acta.* **132**, 145–151 (2000).
24. ICRP. Recommendations of the international commission on radiological protection. *ICRP Publication* **60**, *Annals of the ICRP.* Vol. 21, No. 1–3 (1991).
25. Dubrova, Y. E. *et al.* Further evidence for elevated human minisatellite mutation rate in Belarus eight years after Chernobyl accident. *Mutant. Res.* **281**, 267–278 (1997).
26. Monitoring information of environmental radioactivity level. *Nuclear Regulation Authority.* http://radioactivity.nsr.go.jp/ja/contents/8000/7312/24/20130318air.pdf
27. ICRP. Environmental protection: the concept and use of reference animals and plants. *ICRP publication* **108** (2008).
28. Yamashiro, H. *et al.* Freezability of rat epididymal sperm induced by raffinose in modified Krebs-Ringer bicarbonate (mKRB) based extender solution. *Cryobiology* **55**, 285–294 (2007).

Acknowledgments

We express our gratitude to the Iwaki Livestock Hygiene Service Centre in Fukushima Prefecture, especially to DVM. Yuji Kobayashi and livestock farmers in the 20-km FNPP evacuation zone. We would also like to thank Drs. M. Chiba, Y. Suzuki, A. Shumizu, A. Takahashi, H. Hotta, H. Tamura, and graduate and medical students of Tohoku University. This work was partly supported by a grant for Manabu Fukumoto of the Japan Society for the Promotion of Science, and the Emergency Budget for the Reconstruction of Northeastern Japan, MEXT, Japan, Discretionary Expense of the President of Tohoku University and Nippon Life Insurance Foundation supported this study. This work was also supported by the Programme for Promotion of Basic and Applied Researches for Innovations in Bio-oriented Industry.

Author contributions

H.Y., Y.A., T.F., Y.K., Y.Ku., Mo.F., S.T., M.S., J.K., H.S., T.S., E.I., and M.F. collected specimens; H.Y., E.S., E.I., and M.F. designed the study; H.Y., Y.A., T.F., Y.K., I.K., S.Y., E.U., B.T., T.Y., and M.F. analysed the data; and H.Y. and M.F. wrote the paper.

Additional information

Competing financial interests: The authors declare no competing financial interests.

How to cite this article: Yamashiro, H. *et al.* Effects of radioactive caesium on bull testes after the Fukushima nuclear plant accident. *Sci. Rep.* **3**, 2850; DOI:10.1038/srep02850 (2013).

Digestive Diseases

Dig Dis 2013;31:440–446
DOI: 10.1159/000355242

Hypothermia Protects against Fulminant Hepatitis in Mice by Reducing Reactive Oxygen Species Production

Toshiharu Sakurai[a] Masatoshi Kudo[a] Tomohiro Watanabe[b] Katsuhiko Itoh[c] Hiroaki Higashitsuji[c] Tadaaki Arizumi[a] Tatsuo Inoue[a] Satoru Hagiwara[a] Kazuomi Ueshima[a] Naoshi Nishida[a] Manabu Fukumoto[d] Jun Fujita[c]

[a]Department of Gastroenterology and Hepatology, Kinki University School of Medicine, Osakasayama, [b]Center for Innovation in Immunoregulative Technology and Therapeutics and [c]Department of Clinical Molecular Biology, Graduate School of Medicine, Kyoto University, Kyoto, and [d]Department of Pathology, Institute of Development, Aging and Cancer, Tohoku University, Sendai, Japan

Key Words
Reactive oxygen species · Fulminant hepatitis · Hypothermia · Cold-inducible RNA-binding protein · Cold shock

Abstract
Objective: Mild hypothermia (32–33°C) shows protective effects in patients with brain damage and cardiac arrest. Although cold-inducible RNA-binding protein (CIRP) contributes to the protective effects of hypothermia through extracellular signal-regulated kinase activation in fibroblasts, the effects of hypothermia in the liver remain unclear. ***Methods:*** We analysed the effects of cold temperature on fulminant hepatitis, a potentially fatal disease, using the D-galactosamine (GalN)/lipopolysaccharide (LPS) and concanavalin (con) A-induced hepatitis models in mice. After GalN/LPS administration and anaesthesia, mice in the hypothermia group were kept at 25°C and those in control group were kept at 35°C. After concanavalin A (con A) administration, the mice in the hypothermia group were placed in a chamber with an ambient temperature of 6°C for 1.5 h. ***Results:*** Hypothermia attenuated liver injury and prolonged survival. Activation of c-Jun N-terminal kinase and Akt, which are involved in reactive oxygen species (ROS) accumulation, was suppressed by low temperature. Hypothermia significantly decreased oxidized protein levels, and treatment with N-acetyl-L-cysteine, an antioxidant, attenuated GalN/LPS-induced liver injury. In con A-induced hepatitis, CIRP expression was upregulated and Bid expression was downregulated, resulting in decreased apoptosis of hepatocytes in the hypothermia group. ***Conclusions:*** These data suggest that hypothermia directly protects hepatocytes from cell death via reduction of ROS production in fulminant hepatitis.

Introduction

Mild hypothermia has been reported to protect central neurons from ischemic damage [1–3]. Although clinical application of mild hypothermia (32–35°C) for patients with brain injury and cardiac arrest has been conducted

KARGER

E-Mail karger@karger.com
www.karger.com/ddi

0257–2753/13/0316–0440$38.00/0

Dr. Toshiharu Sakurai
Department of Gastroenterology and Hepatology, Faculty of Medicine, Kinki University
377-2 Ohno-Higashi
Osakasayama, Osaka 589-8511 (Japan)
E-Mail sakurai@med.kindai.ac.jp

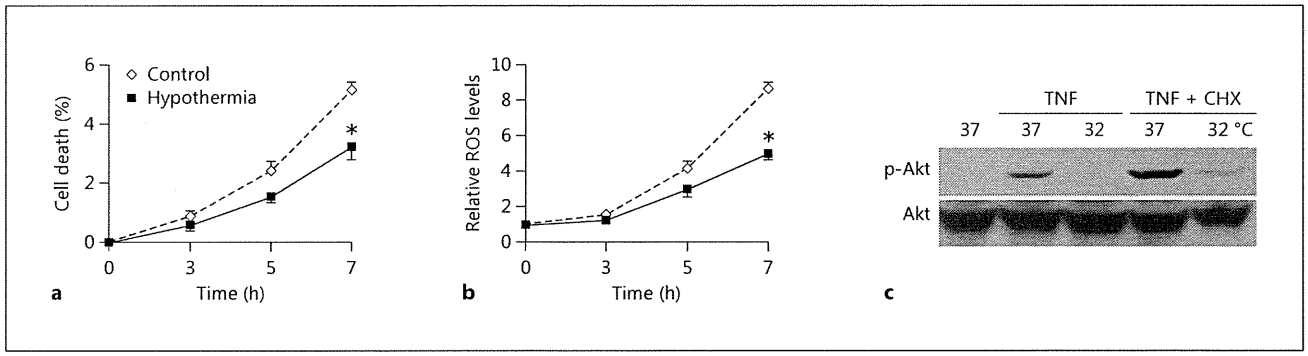

Fig. 1. Low temperature (32°C) reduced ROS production and cell death in TNF-α-treated cells. HeLa cells were cultured at 37 (control) or 32°C (hypothermia) in media containing TNF-α (50 ng/ml) and/or CHX (10 μg/ml). **a**, **b** The cell survival rates and relative ROS levels were examined at the indicated times after initiation of TNF-α treatment. The number of viable cells was estimated by the Trypan blue assay. ROS accumulation was assessed using 5-[and-6]-chloromethyl-2′,7′-dichlorodihydrofluorescein diacetate (CM-H_2DCFDA). The values are shown relative to non-treated cells; results are the mean ± SEM. * $p < 0.05$ versus culture at 37°C (control). **c** After treatment with TNF-α or TNF-α plus CHX, cell lysates were prepared and analysed by Western blotting using the indicated antibodies.

with promising results [4], the molecular mechanisms underlying the protective effects of hypothermia are unknown. In endothelial cells kept under hypothermic conditions, significant upregulation of the anti-apoptotic protein Bcl-2 has been reported. Hypothermia decreased the levels of inflammatory chemokines such as IL-8, MCP-1 and COX-2, which could lead to reduced leukocyte recruitment [5]. Low temperature protects mammalian cells from apoptosis initiated by various stimuli in vitro [6]. Cold-inducible RNA-binding protein (CIRP), a protein induced by mild hypothermia, protects against tumour necrosis factor (TNF)-α-induced apoptosis via activation of extracellular signal-regulated kinase (ERK) [7].

Fulminant hepatitis, resulting from the acute hepatitis caused by viral infection, alcohol or drugs, is associated with high mortality, and development of a new therapy is necessary. This pathophysiological disturbance is caused by excessive hepatocyte death, in which TNF-α plays an important role [8]. Reactive oxygen species (ROS) are another major mediator of inflammation and reduction of ROS levels leads to attenuation of hepatic injury [9]. Akt activation increases intracellular ROS levels [10]. ROS accumulation inhibits mitogen-activated protein kinase (MAPK) phosphatases, resulting in prolonged c-Jun N-terminal kinase (JNK) activation, which contributes to ROS accumulation and hepatocyte death [11]. Here, we analysed the effects of hypothermia on fulminant hepatitis using murine hepatitis models.

Materials and Methods

Cell Culture

Human HeLa cells were maintained in Dulbecco's modified Eagle medium supplemented with 10% foetal bovine serum at 32 or 37°C in a humidified atmosphere of 5% CO_2 in air. For induction of cell death, confluent cultures of cells were incubated with TNF-α (50 ng/ml) in the presence of cycloheximide (CHX; 10 μg/ml). The number of viable cells was estimated by Trypan blue assay. To assess intracellular ROS levels, TNF-α-treated cells were resuspended in PBS containing 10 μM 5-[and-6]-chloromethyl-2′,7′-dichlorodihydrofluorescein diacetate (CM-H_2DCFDA; Invitrogen, Carlsbad, Calif., USA), maintained at 37°C in the dark for 30 min, and analysed by flow cytometry.

Western Blot Analysis

Western blot analysis was performed as previously described [12]. The antibodies used were as follows: anti-phospho Akt, anti-Akt, anti-phospho-JNK, anti-JNK, anti-phospho-ERK, anti-ERK (Cell Signaling Technology, Danvers, Mass., USA), anti-Bcl-2, anti-Bad, anti-Bid (BD Transduction Laboratory, Lexington, Ky., USA), anti-β-actin (Sigma, St. Louis, Mo., USA), anti-Bcl-xL and anti-HNF-3γ (Santa Cruz Biotechnology, Santa Cruz, Calif., USA). Rabbit polyclonal antibody recognizing C terminus of mouse CIRP was prepared as described [13]. To quantify ROS accumulation, an OxyBLOT™ Protein Oxidation Detection Kit (Millipore, Billerica, Mass., USA) was used.

Fulminant Hepatitis Model

C57BL/6 mice, 4–12 weeks old, were purchased from Japan SLC (Shizuoka, Japan) and were kept at 25°C and 55% relative humidity in a 12-hour day/night cycle with free access to food and water. To induce hepatitis, D-galactosamine (GalN; 1,000 mg/kg, Sigma) and lipopolysaccharide (LPS; 0.1 or 35 μg/kg, Sigma) were injected i.p. Thereafter, mice were anesthetized with urethane or

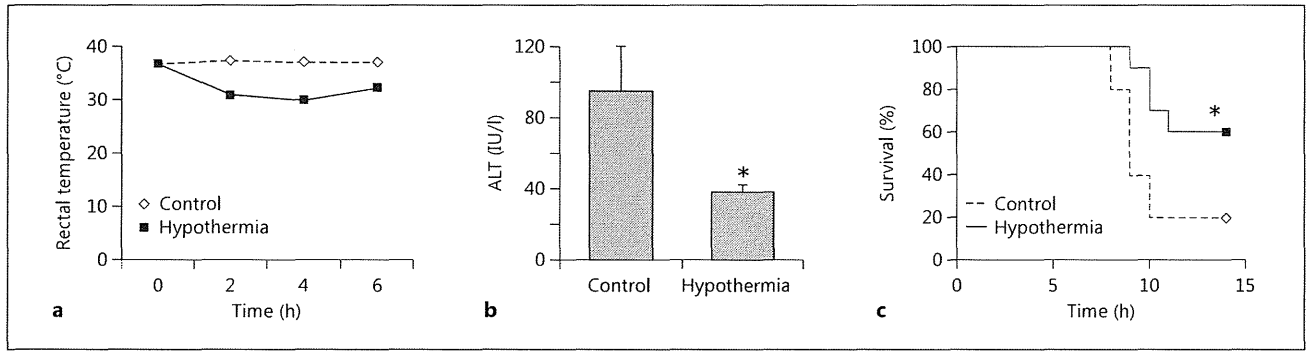

Fig. 2. Hypothermia ameliorates GalN/LPS-induced hepatitis. **a** Rectal temperatures of mice in the control (n = 10) and hypothermia (n = 10) groups were monitored after injection of GalN (1,000 mg/kg) and LPS (0.1 μg/kg); results are the mean. **b** Mice were injected with GalN (1,000 mg/kg) and LPS (0.1 μg/kg), and 8 h after the injection serum ALT levels were examined; results are the mean ± SEM. * $p < 0.05$ versus the control. **c** After injection with GalN (1,000 mg/kg) and LPS (35 μg/kg), the survival rates of mice in the control group (n = 10) and those in the hypothermia group (n = 10) were examined. The difference in the survival rate was analysed by the Kaplan-Meier method and log-rank test. * $p < 0.05$ versus the control.

pentobarbital and divided into 2 groups: mice placed in a chamber with an ambient temperature of 25°C (hypothermia group) and those placed on a plate of 35°C (control group). To investigate the protective effects of N-acetyl-L-cysteine (NAC; Sigma), which is an antioxidant, mice were administered with NAC (150 mg/kg, i.p.) 30 min before GalN/LPS administration (1,000 mg/0.1 μg/kg, i.p.). NAC dissolved in PBS was neutralized before injection. The volume of insensible perspiration was 15 ml/kg/day and increased by 15% per 1°C upshift of body temperature [14]. The volume of PBS as calculated was injected i.p. into mice in the control group to reduce the effect of dehydration.

Concanavalin A (con A; Sigma) was dissolved in sterile saline and injected into the tail vein at a final volume of 200 μl. To examine the effect of hypothermia on their survival, the mice were treated with con A at a lethal dose of 35 mg/kg body weight and divided into 2 groups. One hour after con A injection, the mice in the hypothermia group were placed in a chamber with an ambient temperature of 6°C for 1.5 h. Then, all mice were observed at 22°C. For histological and gene expression analyses, mice were treated with 25 mg/kg of con A, divided into 2 groups, and euthanised at 24 h after con A injection.

This work was conducted under the Japanese Law Concerning the Care and Control of Animals and was approved by the Animal Research Committee of the Faculty of Medicine of Kinki and Kyoto University.

Histopathological Examination

The liver was removed and fixed in 10% formalin, embedded in paraffin and sliced into 5-μm sections for light microscopy. Immunohistochemistry was performed using ImmPRESS™ reagents (Vector Laboratory, Burlingame, Calif., USA) according to the manufacturer's recommendations. The number of proliferating cells was estimated by staining the sections with a mouse monoclonal anti-proliferating cell nuclear antigen (PCNA) antibody (Cell Signaling Technology). TUNEL staining was performed using tissue sections with an in situ Apoptosis Detection Kit (Takara, Tokyo, Japan).

Statistical Analysis

Data are presented as the mean ± SEM. Statistical differences between sample means were calculated by analysis of variance, followed by unpaired Student's t test. To compare the survival rates between groups of mice, the log-rank test was used. $p < 0.05$ was considered significant.

Results

Low Temperature (32°C) Reduced ROS Production and Cell Death in TNF-α-Treated Cells

Treatment with TNF-α and CHX induced death of HeLa cells cultured at 37°C within 6 h (fig. 1a). The number of surviving cells was significantly higher when cells were cultured at 32°C (hypothermia) than when they were cultured at 37°C (control). Similar results were obtained with the human hepatoma cell line HuH-7 [7]. Decreased H_2O_2 accumulation in cells cultured at 32°C was detected using the ROS indicator 5-[and-6]-chloromethyl-2′,7′-dichlorodihydrofluorescein diacetate (CM-H_2DCFDA; fig. 1b). Akt activation promotes ROS production [10]. At 60 min after treatment with TNF-α, the protein level of phospho-Akt was lower in HeLa cells cultured at 32°C than in cells cultured at 37°C (fig. 1c).

Hypothermia Ameliorates GalN/LPS-Induced Hepatitis

The mean rectal temperature was kept at approximately 30°C in the hypothermia group and at 37°C in the control group (fig. 2a). As shown in fig. 2b and c, hypothermic treatment significantly reduced hepatic injury and improved the survival rate in GalN/LPS-induced hepatitis.

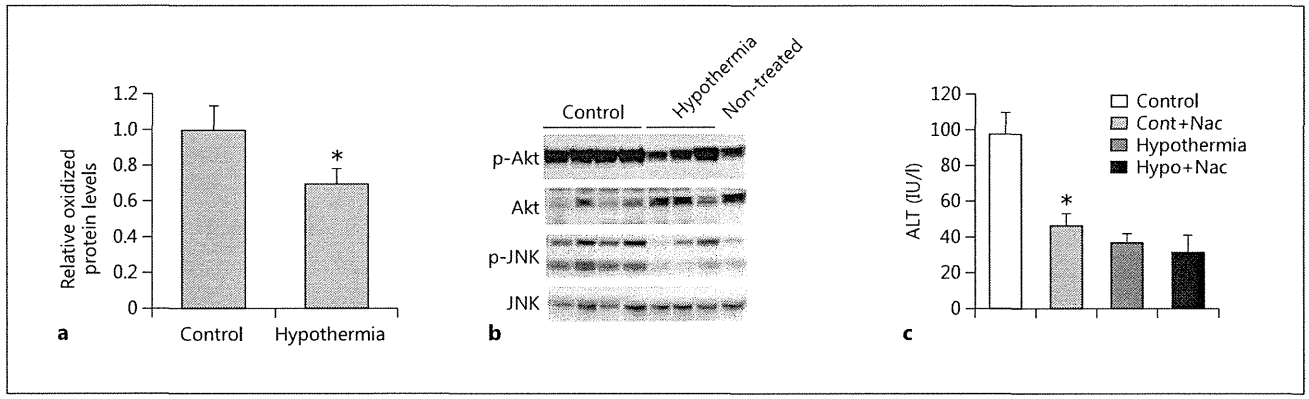

Fig. 3. Hypothermia reduces ROS accumulation in GalN/LPS-treated livers. Mice in the control (n = 8) and hypothermia (n = 8) groups were injected with GalN (1,000 mg/kg) and LPS (0.1 μg/kg), and 24 h after the GalN/LPS injection, tissue lysates were extracted. **a** ROS accumulation was assessed using the OxyBLOT™ Protein Oxidation Detection Kit; the results are the mean ± SEM. * $p < 0.05$ versus the control. **b** Tissue lysates were analysed by Western blotting using the indicated antibodies. **c** Mice in the control group (n = 8) and hypothermia group (n = 8) were injected with GalN (1,000 mg/kg) and LPS (0.1 μg/kg). Mice received NAC (150 mg/kg, i.p.) in the control group (Cont+Nac; n = 8) and the hypothermia group (Hypo+Nac; n = 8) 30 min before GalN/LPS administration (1,000 mg/0.1 μg/kg, i.p.). Eight hours after the GalN/LPS injection, the mice were euthanised and serum ALT levels were examined; results are the mean ± SEM. * $p < 0.05$ versus the control.

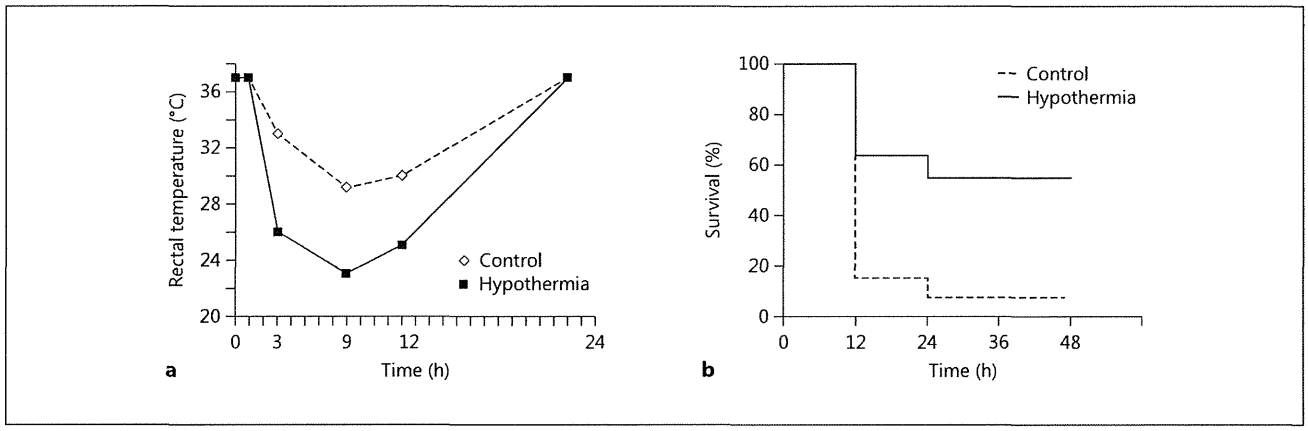

Fig. 4. Hypothermia improves the survival rate in con A-induced hepatitis. **a** Rectal temperatures of mice in the control (n = 14) and hypothermia (n = 11) groups were monitored after injection of con A (35 mg/kg); results are the mean. **b** After injection with con A (35 mg/kg), the survival rates of mice in the control group (n = 14) and those in the hypothermia group (n = 11) were examined. The difference in the survival rate was analysed by the Kaplan-Meier method and log-rank test.

Hypothermia Reduces ROS Accumulation in GalN/LPS-Treated Livers

Mice in the hypothermia group were found to have lower levels of oxidized protein than those in the control group (fig 3a). ROS accumulation inhibits MAPK phosphatases, resulting in prolonged JNK activation, which contributes to hepatocyte death [11]. Accordingly, Akt and JNK activity were decreased in hypothermia-treated livers (fig. 3b). To evaluate the contribution of oxidative stress to GalN/LPS-induced liver damage, we injected the antioxidant NAC. NAC-treated mice showed a significant reduction in GalN/LPS-induced liver injury (fig. 3c). Thus, hypothermia reduces GalN/LPS-induced hepatocyte death through mechanisms that may depend on attenuated ROS accumulation.

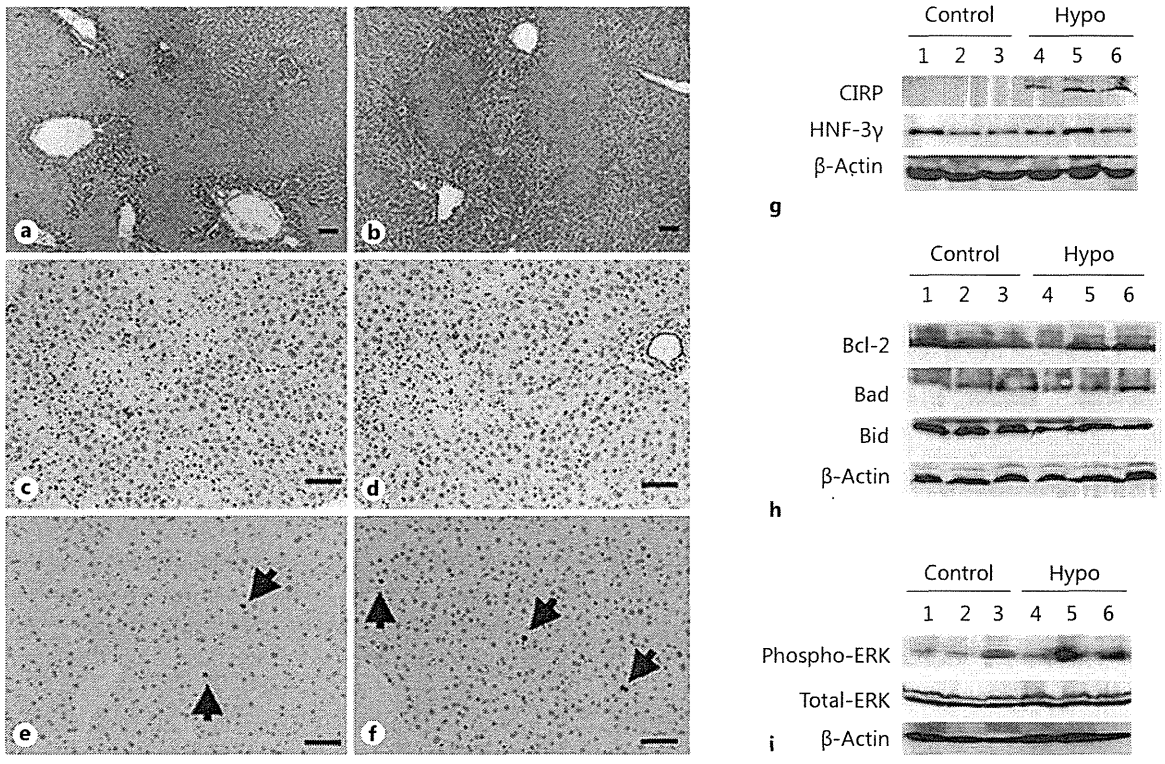

Fig. 5. Hypothermia upregulates CIRP in con A-induced hepatitis. **a–f** Liver histology. Mice were injected with 25 mg/kg body weight of con A. One hour later, the ambient temperature was changed to 25°C (**a**, **c**, **e**) or 6°C (**b**, **d**, **f**) for 1.5 h, and then returned to room temperature. Twenty-four hours after the injection, the mice were euthanised and liver sections were obtained after fixation. Haematoxylin and eosin staining (**a**, **b**); TUNEL staining (**c**, **d**); immunohistochemical staining with mouse anti-PCNA antibody and horseradish peroxidase-conjugated anti-mouse antibody (**e**, **f**). Arrows indicate PCNA-positive cells. Scale bar = 50 μm. **g–i** Gene expression. Groups of mice were treated as above, and the expression of CIRP and HNF-3γ (**g**), Bcl-2 family members (**h**) and ERK (**i**) in the livers of control mice and hypothermic mice (Hypo) was analysed by Western blotting using the indicated antibodies. Results with representative samples are shown.

Hypothermia Upregulates CIRP Expression and Improves the Survival Rate in con A-Induced Hepatitis

TNF-α has been suggested to be a crucial factor in fulminant hepatitis [8]. In con A-induced hepatitis, a mouse model of fulminant hepatitis, the intrahepatic levels of cytokines, including TNF-α, maximally increase 1 h after con A administration [15]. As shown in figure 4, hypothermic treatment improved the survival rate, but the improvement was not significant ($p = 0.096$).

Histological examinations revealed that con A induced severe morphological changes in the liver (fig. 5a). Dilatation of veins and bile ducts was prominent. Massive degenerative lesions consisting of dead parenchymal cells were observed in the midlobular area. The liver of mice in the hypothermia group showed smaller areas of the lesion than the liver of the mice in the control group (fig. 5b). Cells positive for TUNEL staining were localized in the parenchymal cells in the midlobular area and adjacent to the degenerative lesions, and the areas with TUNEL-positive cells were smaller in the hypothermia group (fig. 5c, d). Cold exposure slightly reduced the number of PCNA-positive cells in mice without con A challenge (4.5 ± 1.2 vs. 3.4 ± 0.8 per 1,000 cells). As shown in figure 5e and f, PCNA immunoreactivity was decreased after con A administration in the control and hypothermia groups

to equivalent levels (1.4 ± 0.5 vs. 1.8 ± 0.6 per 1,000 cells). These results suggest that in con A-induced hepatitis, hypothermia improves the survival of mice not by enhancing hepatocyte regeneration but rather by suppressing apoptosis.

The stress response protein CIRP protects cells by activating the ERK pathway [7]. HNF-3γ shows a hepatoprotective effect in acute liver injury [16]. Hypothermia induced the expression of CIRP, but not HNF-3γ, in the livers of con A-treated mice (fig. 5g). As shown in figure 5h, Bid was downregulated in livers in the hypothermia group. There was no difference in the protein levels of XIAP/ILP and other Bcl-2 family members, including Bcl-2, Bcl-xL, Bad and Mcl-1 (fig. 5h and data not shown). The level of phosphorylated ERK was increased in 2 out of 3 examined mice in the hypothermia group (fig. 5i).

Discussion

Fulminant hepatitis is a devastating liver disease with a progressive course and a high mortality rate [17]. Although several studies have shown that mild hypothermia has a protective effect against the encephalopathy resulting from severe liver injury [18], the direct effect of hypothermia on the liver has not been determined. In the present study, we found that hypothermia inhibited apoptosis in the liver and increased the survival rate in mice with con A-induced hepatitis and GalN/LPS-induced hepatitis, which are considered to be relevant to human fulminant hepatitis [19]. Apoptosis is essential for the homeostasis of organs such as the liver [20]. In both human fulminant hepatitis and its animal models, apoptosis of hepatocytes is mediated by death receptors such as Fas (CD95) and the TNF-α receptor [20, 21]. In the death receptor pathway, the pro-apoptotic protein Bid is processed, and its translocation to the mitochondria activates the mitochondrial apoptotic pathway [22]. Bid is required, at least in some cells, for death receptor activation to initiate the apoptosis cascade. Here, we showed that in the livers of mice treated with con A, the Bid protein level was lower in the hypothermia group than in the control group (fig. 5). These results suggest that the protective effect of hypothermia in mice is mediated, at least partly, by the decrease in the Bid protein level in the liver. CIRP blunts TNF-α-mediated apoptosis via ERK activation [7] and inhibits H_2O_2-induced apoptosis through upregulation of thioredoxin expression [23]. CIRP, which was upregulated by hypothermia in this study, may contribute to the anti-apoptotic effects of hypothermia by regulating ERK activity and ROS accumulation in the liver.

Several mechanisms have been proposed to explain the increased resistance of humans and animals to tissue damage as body temperature is reduced. Hypothermia suppresses the production of superoxide anions, nitric oxide and TNF-α in ischemic cells [24]. The hepatic inflammatory response after ischemia is suppressed by hypothermia through selective inhibition of JNK and activator protein-1 [25]. ROS promote TNF-α-induced death and sustained JNK activation by inhibiting MAP kinase phosphatases [11, 26]. Akt activation increases intracellular ROS levels through increased oxygen consumption and by inhibition of the expression of ROS scavengers downstream of FoxO, particularly *sestrin 3* [10]. In the present study, we demonstrated that hypothermia suppressed liver injury and the Akt and JNK pathways in the livers of GalN/LPS-treated mice (fig. 3). Furthermore, mice treated with an antioxidant showed a significant reduction in the severity of liver injury. These data suggest that the attenuation of ROS accumulation is involved in the cyto-protective effect of hypothermia. Further elucidation of the underlying mechanisms of these protective effects will lead to the future development of novel therapeutic modalities.

Acknowledgements

We thank A.M. Park and H. Munakata for technical assistance and discussions. This work was partly supported by Grants-in-Aid from the Ministry of Education, Culture, Sports, Science and Technology of Japan, the Japan Society for the Promotion of Science, Takeda Science Foundation and the Smoking Research Foundation of Japan.

Disclosure Statement

The authors have no conflicts of interest to disclose.

References

1 Curfman GD: Hypothermia to protect the brain. N Engl J Med 2002;346:546.
2 Darby JM: Therapeutic hypothermia after cardiac arrest. N Engl J Med 2002;347:63–65.
3 Wu TC, Grotta JC: Hypothermia for acute ischaemic stroke. Lancet Neurol 2013;12:275–284.
4 Hong MF, Dorian P: Update on advanced life support and resuscitation techniques. Curr Opin Cardiol 2005;20:1–6.

5 Diestel A, Roessler J, Berger F, Schmitt KR: Hypothermia downregulates inflammation but enhances IL-6 secretion by stimulated endothelial cells. Cryobiology 2008;57:216–222.
6 Sakurai T, Itoh K, Liu Y, Higashitsuji H, Sumitomo Y, Sakamaki K, Fujita J: Low temperature protects mammalian cells from apoptosis initiated by various stimuli in vitro. Exp Cell Res 2005;309:264–272.
7 Sakurai T, Itoh K, Higashitsuji H, Nonoguchi K, Liu Y, Watanabe H, Nakano T, Fukumoto M, Chiba T, Fujita J: Cirp protects against tumor necrosis factor-α-induced apoptosis via activation of extracellular signal-regulated kinase. Biochim Biophys Acta 2006;1763:290–295.
8 Bradham CA, Plumpe J, Manns MP, Brenner DA, Trautwein C: Mechanisms of hepatic toxicity. I. TNF-induced liver injury. Am J Physiol 1998;275:G387–G392.
9 Sakurai T, Kudo M, Umemura A, He G, Elsharkawy AM, Seki E, Karin M: p38α inhibits liver fibrogenesis and consequent hepatocarcinogenesis by curtailing accumulation of reactive oxygen species. Cancer Res 2013;73:215–224.
10 Nogueira V, Park Y, Chen CC, Xu PZ, Chen ML, Tonic I, Unterman T, Hay N: Akt determines replicative senescence and oxidative or oncogenic premature senescence and sensitizes cells to oxidative apoptosis. Cancer Cell 2008;14:458–470.
11 Sakurai T, He G, Matsuzawa A, Yu GY, Maeda S, Hardiman G, Karin M: Hepatocyte necrosis induced by oxidative stress and IL-1α release mediate carcinogen-induced compensatory proliferation and liver tumorigenesis. Cancer Cell 2008;14:156–165.
12 Mine H, Sakurai T, Kashida H, Matsui S, Nishida N, Nagai T, Hagiwara S, Watanabe T, Kudo M: Association of Gankyrin and stemness factor expression in human colorectal cancer. Dig Dis Sci 2013;58:2337–2344.
13 Masuda T, Itoh K, Higashitsuji H, Higashitsuji H, Nakazawa N, Sakurai T, Liu Y, Tokuchi H, Fujita T, Zhao Y, Nishiyama H, Tanaka T, Fukumoto M, Ikawa M, Okabe M, Fujita J: Cold-inducible RNA-binding protein (Cirp) interacts with Dyrk1b/Mirk and promotes proliferation of immature male germ cells in mice. Proc Natl Acad Sci USA 2012;109:10885–10890.
14 Guyton AC: Textbook of Medica Physiology, ed 7. Philadelphia, Saunders, 1986.
15 Sass G, Heinlein S, Agli A, Bang R, Schumann J, Tiegs G: Cytokine expression in three mouse models of experimental hepatitis. Cytokine 2002;19:115–120.
16 Nakamura T, Akiyoshi H, Shiota G, Isono M, Nakamura K, Moriyama M, Sato K: Hepatoprotective action of adenovirus-transferred HNF-3γ gene in acute liver injury caused by CCl_4. FEBS Lett 1999;459:1–4.
17 Galun E, Axelrod JH: The role of cytokines in liver failure and regeneration: potential new molecular therapies. Biochim Biophys Acta 2002;1592:345–358.
18 Jalan R: Intracranial hypertension in acute liver failure: pathophysiological basis of rational management. Semin Liver Dis 2003;23:271–282.
19 Tiegs G, Hentschel J, Wendel A: A T cell-dependent experimental liver injury in mice inducible by concanavalin A. J Clin Invest 1992;90:196–203.
20 Galle PR, Hofmann WJ, Walczak H, Schaller H, Otto G, Stremmel W, Krammer PH, Runkel L: Involvement of the CD95 (APO-1/Fas) receptor and ligand in liver damage. J Exp Med 1995;182:1223–1230.
21 Hengartner MO: The biochemistry of apoptosis. Nature 2000;407:770–776.
22 Luo X, Budihardjo I, Zou H, Slaughter C, Wang X: Bid, a Bcl2 interacting protein, mediates cytochrome c release from mitochondria in response to activation of cell surface death receptors. Cell 1998;94:481–490.
23 Li S, Zhang Z, Xue J, Liu A, Zhang H: Cold-inducible RNA binding protein inhibits H_2O_2-induced apoptosis in rat cortical neurons. Brain Res 2012;1441:47–52.
24 Kataoka K, Yanase H: Mild hypothermia – a revived countermeasure against ischemic neuronal damages. Neurosci Res 1998;32:103–117.
25 Kato A, Singh S, Mcleish KR, Edwards MJ, Lentsch AB: Mechanisms of hypothermic protection against ischemic liver injury in mice. Am J Physiol Gastrointest Liver Physiol 2002;282:G608–G616.
26 Kamata H, Honda S, Maeda S, Chang L, Hirata H, Karin M: Reactive oxygen species promote TNFα-induced death and sustained JNK activation by inhibiting MAP kinase phosphatases. Cell 2005;120:649–661.

The Arf GAP SMAP2 is necessary for organized vesicle budding from the *trans*-Golgi network and subsequent acrosome formation in spermiogenesis

Tomo Funaki[a,*], Shunsuke Kon[a,*], Kenji Tanabe[b], Waka Natsume[a], Sayaka Sato[a], Tadafumi Shimizu[a], Naomi Yoshida[a], Won Fen Wong[a], Atsuo Ogura[c], Takehiko Ogawa[d], Kimiko Inoue[c], Narumi Ogonuki[c], Hiromi Miki[c], Keiji Mochida[c], Keisuke Endoh[c], Kentarou Yomogida[e], Manabu Fukumoto[a], Reiko Horai[f], Yoichiro Iwakura[f], Chizuru Ito[g], Kiyotaka Toshimori[g], Toshio Watanabe[h], and Masanobu Satake[a]

[a]Department of Molecular Immunology, Department of Pathology, Institute of Development, Aging and Cancer, Tohoku University, Sendai 980-8575, Japan; [b]Medical Research Institute, Tokyo Women's Medical University, Tokyo 162-8666, Japan; [c]RIKEN Bio Resource Center, Tsukuba 305-0074, Japan; [d]Department of Urology, Yokohama City University Graduate School of Medicine, Yokohama 236-0004, Japan; [e]Department of Food Science and Nutrition, School of Human Environmental Science, Mukogawa Women's University, Nishinomiya 663-8558, Japan; [f]Institute of Medical Science, University of Tokyo, Tokyo 108-8639, Japan; [g]Department of Anatomy and Developmental Biology, Chiba University Graduate School of Medicine, Inohana 260-8670, Japan; [h]Department of Biological Sciences, Nara Women's University, Nara 630-8506, Japan

ABSTRACT The *trans*-Golgi network (TGN) functions as a hub organelle in the exocytosis of clathrin-coated membrane vesicles, and SMAP2 is an Arf GTPase-activating protein that binds to both clathrin and the clathrin assembly protein (CALM). In the present study, SMAP2 is detected on the TGN in the pachytene spermatocyte to the round spermatid stages of spermatogenesis. Gene targeting reveals that *SMAP2*-deficient male mice are healthy and survive to adulthood but are infertile and exhibit globozoospermia. In *SMAP2*-deficient spermatids, the diameter of proacrosomal vesicles budding from TGN increases, TGN structures are distorted, acrosome formation is severely impaired, and reorganization of the nucleus does not proceed properly. CALM functions to regulate vesicle sizes, and this study shows that CALM is not recruited to the TGN in the absence of SMAP2. Furthermore, syntaxin2, a component of the soluble *N*-ethylmaleimide–sensitive factor attachment protein receptor (SNARE) complex, is not properly concentrated at the site of acrosome formation. Thus this study reveals a link between SMAP2 and CALM/syntaxin2 in clathrin-coated vesicle formation from the TGN and subsequent acrosome formation. *SMAP2*-deficient mice provide a model for globozoospermia in humans.

Monitoring Editor
Julie Brill
The Hospital for Sick Children

Received: May 3, 2013
Revised: Jun 14, 2013
Accepted: Jul 1, 2013

This article was published online ahead of print in MBoC in Press (http://www.molbiolcell.org/cgi/doi/10.1091/mbc.E13-05-0234) on July 17, 2013.

*These authors contributed equally to this work.

The authors have no conflicting financial interests.

Address correspondence to: Masanobu Satake (satake@idac.tohoku.ac.jp).

Abbreviations used: Arf GAP, Arf GTPase-activating protein; CALM, clathrin assembly protein; DAPI, 4′,6-diamidino-2-phenylindole; DIC, differential interference contrast; GEF, guanine nucleotide exchanging factor; PAS, periodic acid-Schiff stain; PBS, phosphate-buffered saline; PNA, peanut agglutinin; SNARE, soluble *N*-ethylmaleimide–sensitive factor attachment protein receptor; TEM, transmission electron microscopy; TGN, *trans*-Golgi network; VAMP, vesicle-associated membrane proteins.

INTRODUCTION

The cells of all eukaryotic organisms possess a trafficking system of membrane vesicles that is vital to maintaining cellular homeostasis. It was suggested that the dysregulation of this trafficking is involved in the genesis of tumors as well as in neurodegenerative diseases in humans (McMahon and Boucrot, 2011). As a caveat, in most cases, this hypothesis merely reflects the fact that the gene discovered in one study as responsible for disease onset or progression is known from another study to be involved in vesicle trafficking. Therefore it is not always clear how the possible dysregulation of vesicle trafficking inside the cells might lead to the pathologies seen in particular diseases. One of the reasons for this lack of knowledge is the relatively scant number of studies targeting genes involved in vesicle trafficking.

Clathrin-coated vesicles represent one type of membrane vesicle and are used in a broad range of trafficking pathways, including endocytosis and exocytosis of membrane proteins. The formation of clathrin-coated vesicles is regulated in a coordinated manner by many molecules and Arf proteins, which belong to a family of small GTPases and play key roles in the process (D'Souza-Schorey and Chavrier, 2006; Gillingham and Munro, 2007; Kahn, 2009; Donaldson and Jackson, 2011). The GTPase activity of Arf is activated by an Arf GTPase-activating protein (Arf GAP). Of interest, Arf GAP not only functions as a GAP for Arf but also possesses an Arf-independent function that contributes to the formation of clathrin-coated vesicles (Randazzo and Hirsch, 2004; Spang *et al.*, 2010; Kahn, 2011; Kon *et al.*, 2011).

There are 31 Arf GAP family proteins, and SMAP1 and SMAP2 constitute a small subgroup. SMAPs harbor a clathrin-binding motif and a domain capable of binding to the clathrin assembly protein (CALM; Tanabe *et al.*, 2005, 2006; Natsume *et al.*, 2006). Because of these characteristics, SMAP may exert unique functions in the formation of clathrin-coated vesicles that are not seen in the other Arf GAPs. For example, SMAP1 functions as an Arf6-specific GAP in the endocytosis of the transferrin receptor and is also involved in sorting of endocytosed c-Kit from multivesicular bodies to lysosomes (Tanabe *et al.*, 2005; Kon *et al.*, 2008, 2013). SMAP2 exhibits a similar extent of GAP activity for both Arf1 and Arf6 in vitro. SMAP2 most likely behaves as an Arf1-preferring GAP in cells, however, since the introduction of a GAP-negative mutant of SMAP2 renders cells resistant to brefeldin A, an inhibitor of Arf1 guanine nucleotide exchanging factor (GEF) but not Arf6 GEF (Natsume *et al.*, 2006). Moreover, SMAP2 is localized on early endosomes and the *trans*-Golgi network (TGN) and appears to function in the early endosome–to-TGN transport of TGN46/38 and in the TGN-to–plasma membrane transport of the vesicular stomatitis virus G protein (Natsume *et al.*, 2006; Funaki *et al.*, 2011). Furthermore, SMAP2 can compensate for the lack of SMAP1 in endocytosis of the transferrin receptor (Kon *et al.*, 2013). Therefore SMAP2 may play multiple roles in various intracellular trafficking pathways.

All of the foregoing findings regarding SMAP1 and SMAP2 were obtained using cell cultures in vitro (Tanabe *et al.*, 2005; Natsume *et al.*, 2006; Kon *et al.*, 2008; Funaki *et al.*, 2011). Recently we reported that *SMAP1*-targeted cells have defects in the trafficking of the transferrin receptor as well as c-Kit, and targeted mice are predisposed to develop myelodysplastic syndrome and, eventually, acute myeloid leukemia (Kon *et al.*, 2013). These results demonstrate a possible link between the dysregulated endocytosis in cells and oncogenesis. The TGN functions as a hub organelle in exocytosis by sorting either secreted molecules to the cell membrane or hydrolytic enzymes to lysosomes (Bonifacino and Rojas, 2006). How the functions of tissues/organs would be impaired if the TGN machinery is disrupted is unclear. In this study, to examine the physiological roles of SMAP2 in vivo with respect to TGN transport, we targeted *SMAP2* and found that *SMAP2*-deficient male mice were infertile and exhibited globozoospermia. Vesicle budding from the TGN, as well as acrosome formation, was disorganized in *SMAP2*-deficient spermatogenesis.

RESULTS

Generation of *SMAP2*-deficient mice

We generated *SMAP2*-deficient mice using a gene-targeting method. A *SMAP2*-targeting construct was designed to replace the Met^{init}-containing exon 1 of *SMAP2* with *LacZ* and neomycin-resistance (*neo*^{r}) gene sequences (Figure 1A). Homologous recombination should give rise to a protein consisting of the amino-terminal 12 amino acids of SMAP2 fused in-frame with *LacZ*. We obtained two independent founder mice possessing the germline-transmitted, targeted *SMAP2* allele. Because essentially similar results were obtained for both lines of mice, representative results from one of the lines are described here. To generate *SMAP2*(–/–) mice, *SMAP2*(+/–) F1 mice were mated, and the F2 offspring were genotyped by Southern blot and PCR analysis (Figure 1B). *SMAP2*(+/–) and (–/–) mice were present in the expected Mendelian ratios.

SMAP2 expression was examined in tissues of wild-type mice by Northern blot analyses (Figure 1C). Two transcripts, 2.9 and 1.3 kb, which contain the same open reading frame but differ in their 3′-untranslated regions, were detected in the tissues examined (Figure 1C, top). Because the major phenotype of *SMAP2*(–/–) mice was defective spermatogenesis, as described later, *SMAP2* expression at various stages of spermatogenesis was examined using wild-type testicular cells. *SMAP2* transcripts were detected in pachytene spermatocytes to the round spermatid stages (Figure 1C, bottom). Immunoblot analyses using lysates from brain and testis detected SMAP2 at 47 kDa in the wild-type tissue but not in the *SMAP2*(–/–) tissue (Figure 1D). This result verified the SMAP2 deficiency in the *SMAP2*-targeted mice.

Infertility and globozoospermia seen in *SMAP2*-targeted male mice

SMAP2(–/–) mice grew to adulthood and were apparently healthy, but mating outcomes were not normal. When we conducted cross-breeding experiments using *SMAP2*(–/–) mice (Table 1), we found that female *SMAP2*(–/–) mice were fertile when mated to *SMAP2*(+/–) male mice. Male *SMAP2*(–/–) mice, however, were infertile regardless of the *SMAP2* genotype of the female. Thus male infertility was detected as a phenotype of *SMAP2*-targeted mice.

Epididymides of *SMAP2*(–/–) male mice were examined, and the numbers of sperm present in the epididymides were similar in *SMAP2*(+/–) and (–/–) mice (Table 2). When epididymal sperm were observed by differential interference contrast (DIC) microscopy (Figure 2A), however, a normal hook-shaped head was observed for the *SMAP2*(+/+) sperm, whereas a cylindrical or round head was observed for the *SMAP2*(–/–) sperm. The percentages of sperm possessing hook-shaped and round heads were quantified (Table 2). A majority of *SMAP2*(+/–) sperm possessed the hook-shaped head (94%), whereas most *SMAP2*(–/–) sperm were round headed (79%). Thus the morphology of *SMAP2*(–/–) sperm is typical of globozoospermia (Dam *et al.*, 2007).

Testes were sectioned, stained with hematoxylin–eosin, and examined by light microscopy (Figure 2B). In the seminiferous tubules of *SMAP2*(+/+) testes, many elongated spermatids possessing hook-shaped heads were detected. By contrast, most spermatids in the seminiferous tubules from *SMAP2*(–/–) testes possessed round heads. Similar observations were obtained for epididymal sperm

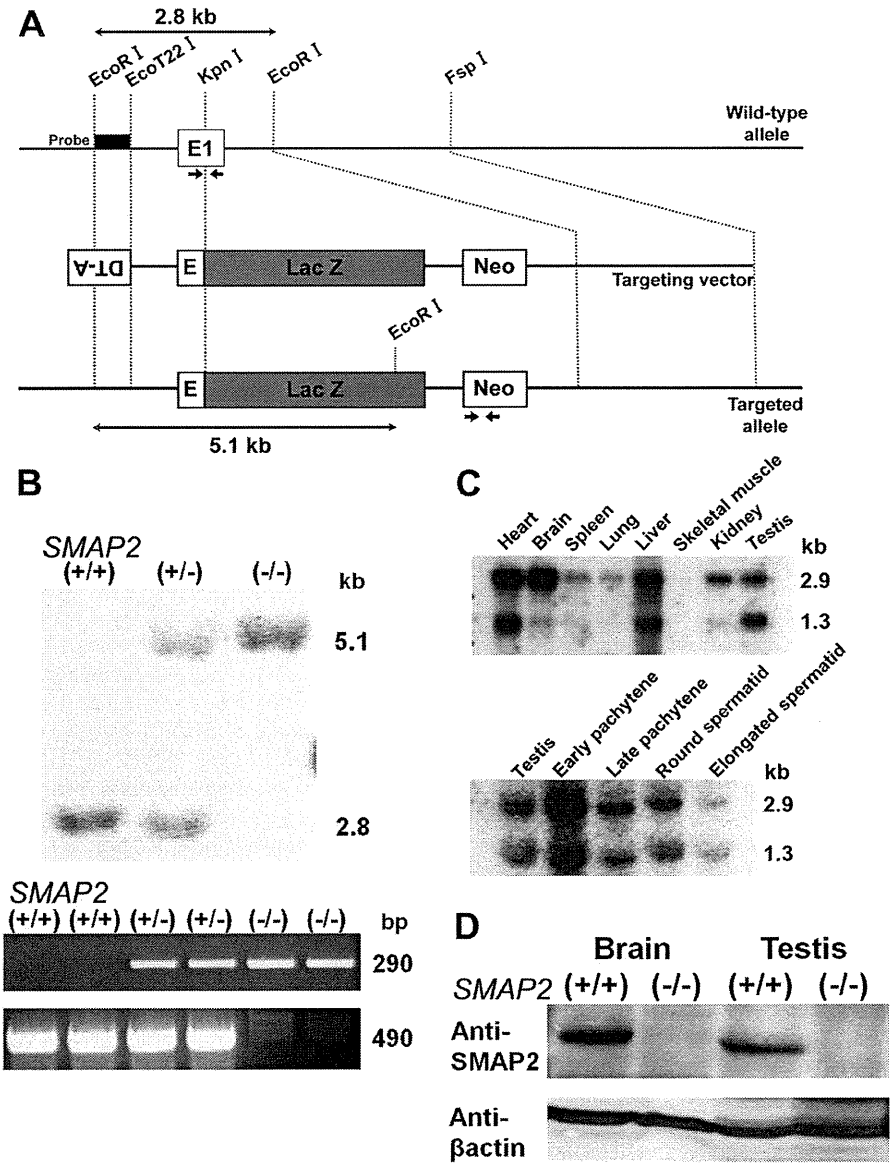

FIGURE 1: Targeting and expression of SMAP2. (A) Schematic diagram of the *SMAP2* gene. The 3′-terminal half of exon 1 in the wild-type allele was replaced by the LacZ gene in the targeted allele. Neo represents the neomycin-resistance gene used as a positive selection marker, and DT-A represents the diphtheria toxin A subunit gene. The probe for Southern blot analysis and the PCR primers used for genotyping are indicated by the rectangle and arrows, respectively. (B) Southern blot (top) and PCR (bottom) analyses of genomic DNAs that were prepared from *SMAP2*(+/+), (+/–), and (–/–) mouse tail snips. For the Southern blot, DNA was digested by *Eco*RI and hybridized by the probe shown in A. For PCR, 290– and 490–base pair bands were amplified from the targeted and wild-type alleles, respectively. (C) Northern blot analysis of RNA prepared from the indicated tissues of wild-type mice (top). Bottom, germ cells from the testes were fractionated into the indicated stages and their RNA processed for Northern blot analysis. The 2.9- and 1.3-kb bands represent *SMAP2* transcripts. (D) Immunoblot analysis of SMAP2. Protein lysates were prepared from brain and testis of *SMAP2*(+/+) and (–/–) mice and immunoblotted with an anti-SMAP2 antibody. β-Actin was used as a loading control.

(Figure 2C). Therefore the globozoospermia seen in epididymal sperm was most likely due to defects in spermatogenesis.

In humans, globozoospermia is characterized by abnormal alignment of mitochondria along the axoneme and malformation and/or lack of an acrosome (Suzuki-Toyota *et al.*, 2004). The distribution pattern of mitochondria in sperm was examined by staining cells with MitoRed (Figure 2D). In wild-type sperm, mitochondria were aligned along the axoneme, whereas in *SMAP2*-deficient sperm, some mitochondria had not moved to the axoneme but remained near the nucleus. Moreover, localization of sp56, a marker for acrosome formation, was very irregular or absent in *SMAP2*(–/–) sperm (Figure 2D). Thus the morphology of *SMAP2*(–/–) sperm indeed corresponds to globozoospermia in humans.

In mouse sperm, energy necessary for sperm motility is supplied from mitochondrial respiration according to some reports (Narisawa *et al.*, 2002; Ford, 2006) or from anaerobic glycolysis according to others (Miki *et al.*, 2004; Mukai and Okuno, 2004; Mukai and Travis, 2012). Structural changes in the mid piece, which contains the mitochondria, are closely associated with sperm motility (Wilton *et al.*, 1992; Mundy *et al.*, 1995; Piomboni *et al.*, 2012). In addition to proper motility, the acrosome reaction is also required for successful fertilization. With this background in mind, we examined the motility and fertilizing capacity of *SMAP2*(–/–) sperm in vitro. Measurements of various motility parameters revealed that the motility of *SMAP2*(–/–) sperm was significantly ($p < 0.05$) reduced compared with that of *SMAP2*(+/–) sperm (Supplemental Table S1). The decreases included percentage of motile sperm, average path velocity, straight-line velocity, curvilinear velocity, amplitude of lateral head displacement, and beat frequency. In vitro fertilization by *SMAP2*(–/–) sperm was evaluated using wild-type oocytes (Supplemental Table S2). The percentage of two-cell embryos derived from *SMAP2*(–/–) sperm was 3.9%, whereas the fertilization rate by *SMAP2*(+/–) sperm was 38%. When intracytoplasmic sperm injection experiments were performed (Supplemental Table S3), however, pups were produced at similar levels by the *SMAP2*(–/–) and (+/–) sperm (59 and 58%, respectively). Taken together, these results indicate that *SMAP2*(–/–) sperm possess a developmentally competent haploid genome but are defective in motility and ability to penetrate the oocyte.

Globozoospermia is intrinsic to *SMAP2*-targeted germ cells

SMAP2 transcripts were detected by Northern blot analyses in testes of *Sl/Sld* mice devoid of germ cells (data not shown). Because interactions between germ cells and somatic supporting cells are necessary for proper spermatogenesis, the impaired head formation in *SMAP2*(–/–) sperm could be caused by defects in the supporting cells. To examine this possibility, we conducted spermatogonial stem cell transplantations. Germ stem cells were prepared from *SMAP2*(–/–) testes

SMAP2 genotype		Number of mating trial	Average number of litters per mating
Male	Female		
(–/–)	(–/–)	4	0
(–/–)	(+/+)	11	0
(+/–)	(–/–)	4	4
(+/+)	(+/+)	4	4

TABLE 1: *SMAP2* genotype and fertility.

and injected into the seminiferous tubules of testes of W/W^v mice that lack germ cells. Three months later, differentiated spermatids were readily detected, but most exhibited the same defective round heads (Supplemental Figure S1, left). In a reciprocal transplantation experiment, germ stem cells were prepared from the testes of pCXN-EGFP transgenic mice and implanted into the seminiferous tubules of busulfan-treated *SMAP2*(–/–) animals whose testes lack germ cells. Spermatids from these transplantations possessed hook-shaped heads and appeared properly differentiated (Supplemental Figure S1, right). These results suggest that the defects causing globozoospermia are likely intrinsic to the *SMAP2*-targeted germ cells and not the supporting cells.

Stage-dependent expression and localization of SMAP2 at the TGN during spermatogenesis

SMAP2 expression during spermatogenesis was examined by immunofluorescence using a testicular cell suspension that was spun down onto microscope slides (Figure 3A). 4′,6-Diamidino-2-phenylindole (DAPI) staining showed the nuclear morphology, as well as chromatin condensation, whereas γH2AX staining detected sites of DNA double-strand breaks. Combined use of DAPI and γH2AX allowed the identification of the stages of spermatogenesis (Xu, 2003; Figure 3A). SMAP2 expression was not detected in spermatogonia or in leptotene spermatocytes but could first be detected in the cytoplasm of zygotene spermatocytes as multiple punctae. In pachytene spermatocytes and round spermatids, SMAP2 fluorescence appeared not only as multiple punctae but also in a single, large focus. SMAP2 fluorescence was absent in elongated spermatids and sperm. Thus SMAP2 expression was stage dependent. Immunofluorescence localization of SMAP2 is consistent with the detection by Northern blot (Figure 1C).

We previously reported that SMAP2 was distributed on early endosomes (as multiple punctae) and on the TGN (as a single large focus) in tissue culture cells (Natsume *et al.*, 2006; Funaki *et al.*, 2011). Therefore we examined whether SMAP2 is similarly localized in spermatogenesis. Double-labeling immunofluorescence was performed on pachytene spermatocytes and round spermatids (Figure 3B). In the single large focus of SMAP2 staining, fluorescence from SMAP2 overlapped with that from TGN38, syntaxin6, and clathrin. Pearson's r was significant ($r > 0.5$) for each combination. In tissue culture cells, clathrin is located on various organelles but is particularly concentrated on the TGN (Huang *et al.*, 2007; Burgess *et al.*, 2011); TGN38 and syntaxin6 are TGN markers (Humphrey *et al.*, 1993; Bock *et al.*, 1997; Roqueta-Rivera *et al.*, 2011). Therefore the single, large, focus-like structure seen in germ cells most likely represents the TGN, and SMAP2 appears to be densely localized there. By contrast, GM130 is a marker of the *cis*-Golgi (Nakamura *et al.*, 1995), and fluorescence from SMAP2 and GM130 did not colocalize ($r < 0.5$). Furthermore, GM130 was located relatively far from the nucleus, whereas SMAP2 was relatively nearer to the nucleus, and this relative localization of SMAP2/TGN and GM130/*cis*-Golgi is in good accord with the known spatial orientation of the Golgi apparatus during spermiogenesis. Namely, rotation of the Golgi relocates the *cis*-Golgi and TGN so that they are oriented toward the cell surface and nucleus, respectively (Hermo *et al.*, 1980).

Aberrant acrosome formation in *SMAP2*-targeted spermiogenesis

We examined the relationship between SMAP2 residing on the TGN and acrosome formation. Acrosome formation occurs in the round and elongated spermatid stages and is divided into the following four phases: a Golgi phase, a cap phase, an acrosome phase, and a maturation phase (Figure 4A). Each phase is characterized by distinct staining patterns of the acrosomal component sp56 (Kim *et al.*, 2001). SMAP2 fluorescence at the TGN was detected in the Golgi and cap phases, and sp56 fluorescence was detected near the nucleus, whereas SMAP2 fluorescence was relatively distant from the nucleus. SMAP2 and sp56 fluorescence did not overlap. This relative localization is consistent with the known spatial orientation of the TGN and the acrosome. SMAP2 fluorescence was not detected in the acrosome and maturation phases. Therefore TGN-associated SMAP2 was detected in the early phases of acrosome formation when acrosomal components are synthesized. The disappearance of SMAP2 probably reflects the shedding of the TGN and other organelles during spermiogenesis (Susi *et al.*, 1971).

Many *SMAP2*(–/–) sperm exhibited globozoospermia, which is closely associated with aberrant acrosome formation (Holstein *et al.*, 1973; Ito *et al.*, 2004; Lin *et al.*, 2007; Roqueta-Rivera *et al.*, 2011). Therefore we examined acrosome formation during *SMAP2*(–/–) spermiogenesis using sp56 as a marker (Figure 4B). Various morphological abnormalities were evident in round and elongated spermatids. In Figure 4B, I, sp56 was not concentrated or fused into one focus but was distributed as multiple discrete spots along the nucleus; sp56 did not form a distinct cap over the nucleus and appeared to consist of a thick aggregate of multiple punctae (Figure 4B, II). The acrosome did not form the typical crescent but was irregular in shape (Figure 4B, III) and often remained separated into discrete foci (Figure 4B, IV). Therefore the *SMAP2* deficiency clearly perturbs acrosome formation. At the light microscopic level, the major perturbation appears to be abnormal fusion of the vesicles carrying the acrosomal components.

To correlate the abnormalities in the acrosome to the phases of acrosome formation, we frozen sectioned testis tissues and stained them with peanut agglutinin (PNA), a lectin that reacts with polysaccharides in the acrosome. Supplemental Figure S2A shows the Golgi

SMAP2 genotype	Number of mice examined	Number of sperm in epididymis ($\times 10^7$)	Number of sperm examined per mouse	Hook-shaped head (%)	Cylindrical or round head (%)
(–/–)	7	3.27 ± 0.68	57	21 ± 16	79 ± 16
(+/–)	4	3.27 ± 0.57	60	94 ± 6.8	6 ± 6.8
p	–	–	–	1E-05	1E-05

TABLE 2: Number of sperm and their morphology.

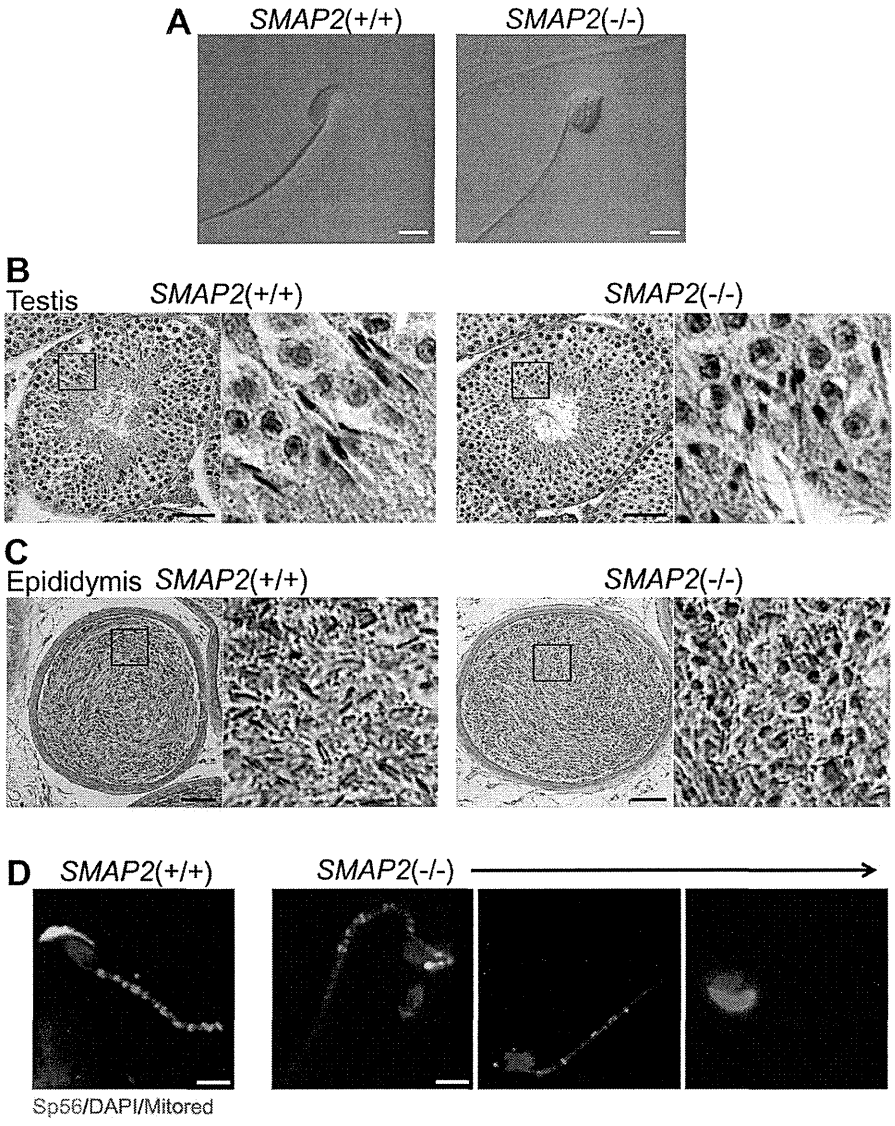

FIGURE 2: Morphology of sperm and spermatids in the epididymis and testis. (A) Sperm were collected from the epididymis of *SMAP2*(+/+) and (–/–) mice and observed using DIC microscopy. (B, C) Testis and epididymis specimens from *SMAP2*(+/+) and (–/–) mice were sectioned, stained with hematoxylin–eosin, and viewed using a light microscope. (D) Sperm from *SMAP2*(+/+) and (–/–) mice were stained with anti-sp56, DAPI, and MitoRed. Bars, 5 μm (A, D), 50 μm (B, C).

through the maturation phase in *SMAP2*(+/+) and (–/–) seminiferous tubules, and confirms the aberrant acrosome formation in *SMAP2*(–/–) cells. Periodic acid-Schiff stain (PAS) staining also revealed the presence of normal-shaped acrosomes in the elongated spermatids from the wild-type but not *SMAP2*(–/–) seminiferous tubules (Supplemental Figure S2B).

Formation of proacrosomal vesicles from the TGN is disrupted in *SMAP2*-targeted spermiogenesis

Acrosome formation is initiated by the budding of proacrosomal vesicles from the TGN. To examine possible abnormalities in this step, we processed testes sections for analysis by transmission electron microscopy (TEM; Figure 5A). In the Golgi phase of acrosome formation, wild-type spermatids (Figure 5A, I) possess an umbrella-shaped TGN, and multiple proacrosomal vesicles of uniform size are present between the TGN and nuclear membrane. By contrast, in *SMAP2*-targeted spermatids (Figure 5A, II), proacrosomal vesicles were present but were not uniform in size and appeared to be larger than those in wild-type cells. In other *SMAP2*-targeted spermatids (Figure 5A, III), the lamellar structure of the TGN formed loose whorls. These observations suggest that there are abnormalities in the budding of vesicles from the TGN in *SMAP2*-targeted cells.

To evaluate the foregoing observations more quantitatively, we measured the diameter of proacrosomal vesicles on the TEM sections. Approximately 20 vesicles per cell and a total of 15 cells were measured for each genotype. Figure 5B (also see Supplemental Figure S3) shows the range of proacrosomal vesicle sizes and confirms that the *SMAP2*-targeted cells tended to produce larger-diameter vesicles than do wild-type cells. Therefore abnormal acrosome formation in *SMAP2*-targeted cells appears to involve budding of proacrosomal vesicles from the TGN.

Formation of the acrosome from proacrosomal vesicles is disrupted in *SMAP2*-targeted spermiogenesis

The later phases of acrosome formation were examined by TEM (Figure 6). In the cap phase in wild-type cells (Figure 6, I), proacrosomal vesicles that had budded from the TGN fused with each other and formed a large acrosome (Ac) located at the acroplaxome (Apx), a unique substructure composed of keratin and actin that serves as a site for anchoring the acrosome to the nuclear membrane (Kierszenbaum *et al.*, 2003). By contrast, in a cap-phase *SMAP2*-targeted cell (Figure 6, II), acrosomes of intermediate size were formed but never fused to form one large acrosome and remained as multiple pseudoacrosomes (indicated by the arrows). These pseudoacrosomes attached to multiple sites on the nuclear envelope. In another *SMAP2*-targeted cell (Figure 6, III), one acrosome appeared to be formed but was greatly enlarged in size (the TGN was also disorganized and partly distended; arrows). These observations indicate that acrosome formation from proacrosomal vesicles in *SMAP2*-deficient cells is disrupted, even though the acroplaxome structures are well organized on the nuclear lamina. Therefore it is unlikely that a defect in the acroplaxome caused the aberrant acrosome formation.

Secondary abnormalities in spermiogenesis in *SMAP2*-deficient cells

In the acrosome phase in wild-type cells (Figure 6, IV), the acrosome was detected as a long and continuous layer along the nuclear membrane. In the enlargement of marginal rings (arrowhead), ectoplasmic specializations (two white arrows) derived from Sertoli cells cover the surface of the acrosome. A manchette structure is also

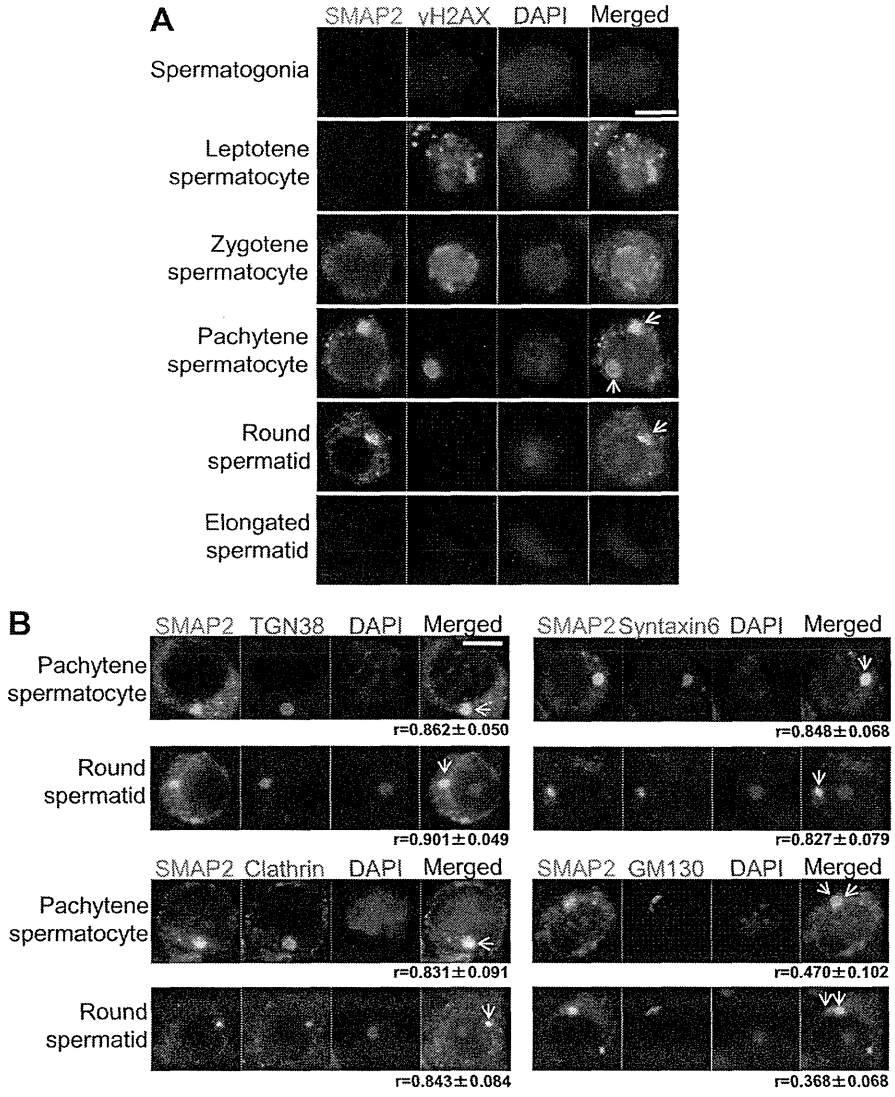

FIGURE 3: Expression and subcellular location of SMAP2 during spermatogenesis as detected by immunofluorescence staining. Single-cell suspensions were prepared from seminiferous tubules of wild-type testes, centrifuged onto glass slides, and fixed. (A) The cells were stained with anti-SMAP2, anti-γH2AX, and DAPI. Based on the staining pattern of the nuclear γH2AX and DAPI, differentiation stages were assigned as indicated. (B) The cells were stained as indicated. Pachytene spermatocytes and round spermatids are shown. Clathrin is the vesicle marker, TGN38 and syntaxin6 are TGN markers, and GM130 is a *cis*-Golgi marker. Bar, 5 μm. Values of *r* (average ±SD) represent the Pearson's coefficients quantifying the degree of colocalization between SMAP2 and the various marker proteins. For $r > 0.5$, colocalization is significant.

observed (asterisk). In a *SMAP2*(–/–) cell (Figure 6, V), however, the ectoplasmic specializations were interrupted (arrow), and the acrosome appeared swollen near the marginal ring (arrowhead). In another *SMAP2*(–/–) cell (Figure 6, VI), a space between the acrosome and nucleus appeared to be filled with a Sertoli cell protrusion (Sc; arrow).

Finally, in the maturation phase in wild-type cells (Figure 6, VII), the ectoplasmic specialization (two white arrows) and the manchette (asterisk) were observed, but in a *SMAP2*(–/–) cell (Figure 6, VIII), the nucleus appeared fragmented, the acrosome was dispersed (arrows), and the manchette was located ectopically (asterisk). An invagination of the manchette into the nucleus was observed in another *SMAP2*(–/–) cell (Figure 6, IX). Finally, in *SMAP2*(–/–) sperm from the epididymis, the shedding of cytoplasmic content appeared to be incomplete, since many mitochondria were detected near the nucleus (Figure 6, XI). These alterations in the acrosome and maturation phases in *SMAP2*-deficient sperm may be secondary events that result from the defects in proacrosomal vesicle budding and acrosome formation.

Molecules involved in the formation of proacrosomal vesicles

The proacrosomal vesicles budding from the TGN in *SMAP2*(–/–) spermatids had larger diameters than those in the wild-type cells (Figure 5). CALM is a protein that affects the size of clathrin-coated vesicles, since vesicles become enlarged in cells lacking *CALM/AP180* (Zhang *et al.*, 1998; Nonet *et al.*, 1999; Meyerholz *et al.*, 2005). In addition, we previously reported a physical association between SMAP2 and CALM (Natsume *et al.*, 2006). Therefore, to explore a possible link between SMAP2 and the vesicle size, we performed double immunofluorescence of SMAP2 and CALM using a germ cell suspension (Figure 7A). In wild-type spermatocytes and round spermatids, SMAP2 was concentrated at the TGN, as described earlier, whereas CALM fluorescence was detected diffusely in the cytoplasm but also colocalized with SMAP2. In the *SMAP2*(–/–) cells, CALM was no longer localized to the TGN (the overall amount of CALM was not affected by SMAP2 deficiency; data not shown). When the wild-type and *SMAP2*(–/–) germ cells were mixed at a 1:1 ratio, CALM was colocalized with SMAP2 at the TGN in the wild-type cells but homogenously distributed in the *SMAP2*(–/–) cells. Thus mobilization of CALM to the TGN appears to be dependent on SMAP2.

We also used coimmunoprecipitation to confirm a physical association between SMAP2 and CALM (Figure 7B). Lysates were prepared from wild-type testes and immunoprecipitated with an anti-CALM antibody. Immunoblotting of the precipitate with an anti-SMAP2 antibody revealed the presence of SMAP2, indicating an association between CALM and SMAP2.

An important implication of the observations of acrosome formation (Figure 6) is that some process in the fusion of proacrosomal vesicles was impaired in the *SMAP2*(–/–) cells. Syntaxin2 is a component of the soluble *N*-ethylmaleimide–sensitive factor attachment protein receptor (SNARE) complex, which serves as the fusion machinery for proacrosomal vesicles (Rizo and Sudhof, 2002; Roqueta-Rivera *et al.*, 2011). In Figure 7C, cells were double stained for syntaxin2 and sp56. In wild-type spermatocytes, syntaxin2 was concentrated at foci in the cytoplasm. In round spermatids, syntaxin2 was detected adjacent to the sp56 fluorescence. In contrast, in the *SMAP2*(–/–) cells, although syntaxin2 was concentrated at foci during the spermatocyte stage, during the round spermatid stage

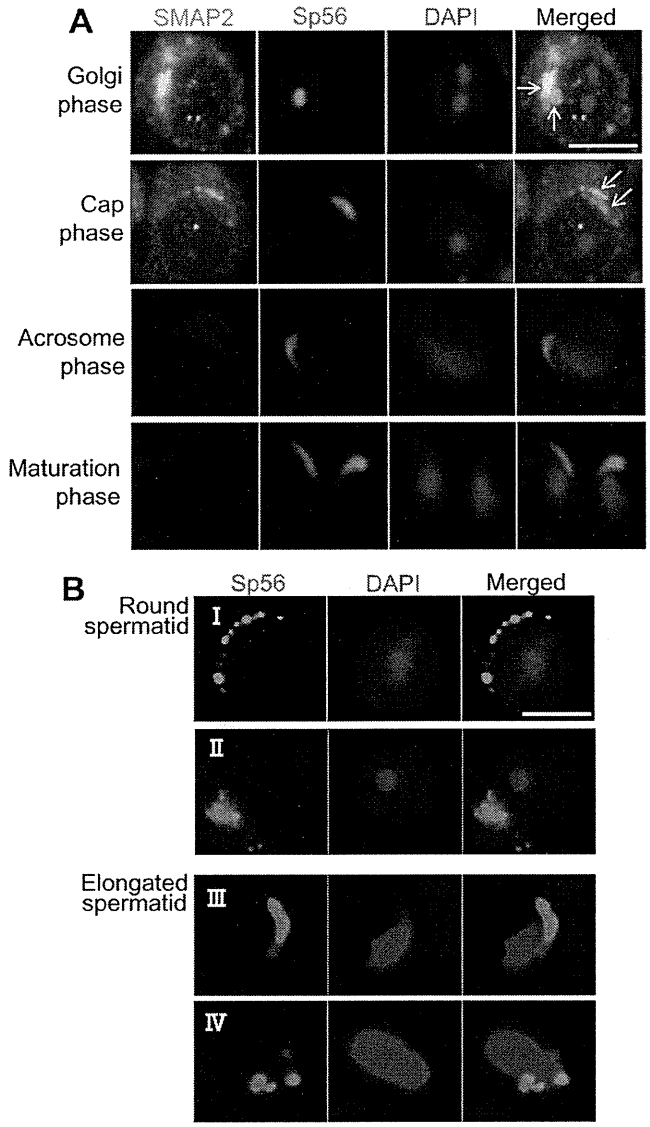

FIGURE 4: Acrosome formation and SMAP2. (A) Germ cells were prepared from wild-type testes as in Figure 3 and processed for immunofluorescence staining as indicated. Each row represents a stage of acrosome formation (Golgi, cap, acrosome, and maturation phases). The marker for the acrosomal components is sp56. (B) Germ cells were prepared from *SMAP2*(–/–) testes and processed for sp56 staining. See the text for details of observed abnormalities. Bars, 5 μm.

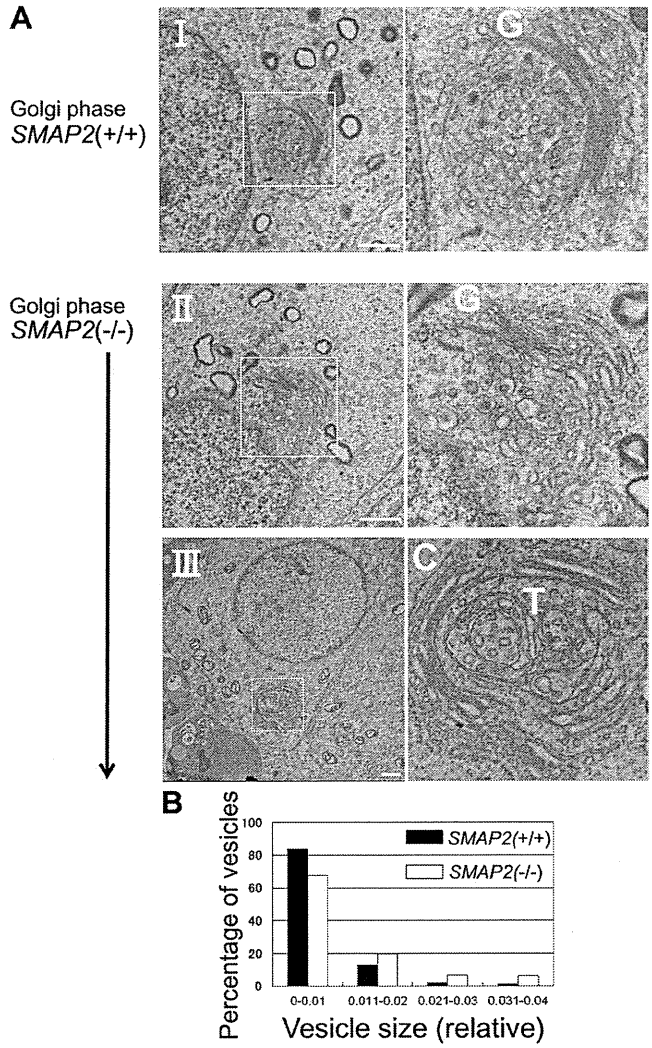

FIGURE 5: Electron microscopic observations of proacrosomal vesicle formation at the Golgi phase. (A) Germ cells from *SMAP2*(+/+) and (–/–) mice were processed for electron microscopic observations. C, *cis*-Golgi network; G, Golgi apparatus; T, *trans*-Golgi network. Bars, 1 μm. (B) Size distribution of proacrosomal vesicles observed in *SMAP2*(+/+) (closed bars) and (–/–) (open bars) germ cells at the Golgi phase. Using the images shown in A, we measured diameters for each proacrosomal vesicle. The areas of the vesicles were calculated using image-processing software and divided by the square of the magnification. The diameters are presented in relative units. Vesicle sizes are binned as indicated. See Supplemental Figure S3 for the detailed size distribution of vesicles.

syntaxin2 was irregularly distributed in the cytoplasm and had no discernible correlation with sp56 fluorescence. This result suggests that the SNARE complex may not be properly engaged in the fusion events in *SMAP2*-deficient germ cells. Syntaxin2 was not detected in CALM immunoprecipitates of wild-type cells (Figure 7B).

Finally, the relative orientation of syntaxin2 to TGN38 was examined by double labeling (Figure 7D). In wild-type spermatocytes, focal fluorescence of syntaxin2 partly overlapped with that of TGN38. In wild-type round spermatids, syntaxin2 localization was distinct from TGN38. Of note, syntaxin2 was located closer to the nucleus, whereas TGN38 was detected further from the nucleus. The observations are consistent with the scenario that syntaxin2 originates from the TGN and then moves to the site of proacrosomal vesicle fusion. Such features were never observed in *SMAP2*(–/–) spermatids.

DISCUSSION

In this study we showed that *SMAP2*-deficient male mice are infertile. Sperm in the testes and epididymides in these mice exhibit morphological abnormalities indicative of globozoospermia, a phenotype seen also in infertile men. Formation of the acrosome is disrupted in *SMAP2*-deficient sperm, and several reports suggested that defects in acrosome formation cause globozoospermia (Holstein *et al.*, 1973; Ito *et al.*, 2004; Lin *et al.*, 2007; Roqueta-Rivera *et al.*, 2011). Therefore the globozoospermia seen in the *SMAP2* deficiency is likely due to defects in acrosome formation.

During spermiogenesis, a large number of proacrosomal vesicles bud from the TGN, fuse with each other, anchor to the nuclear

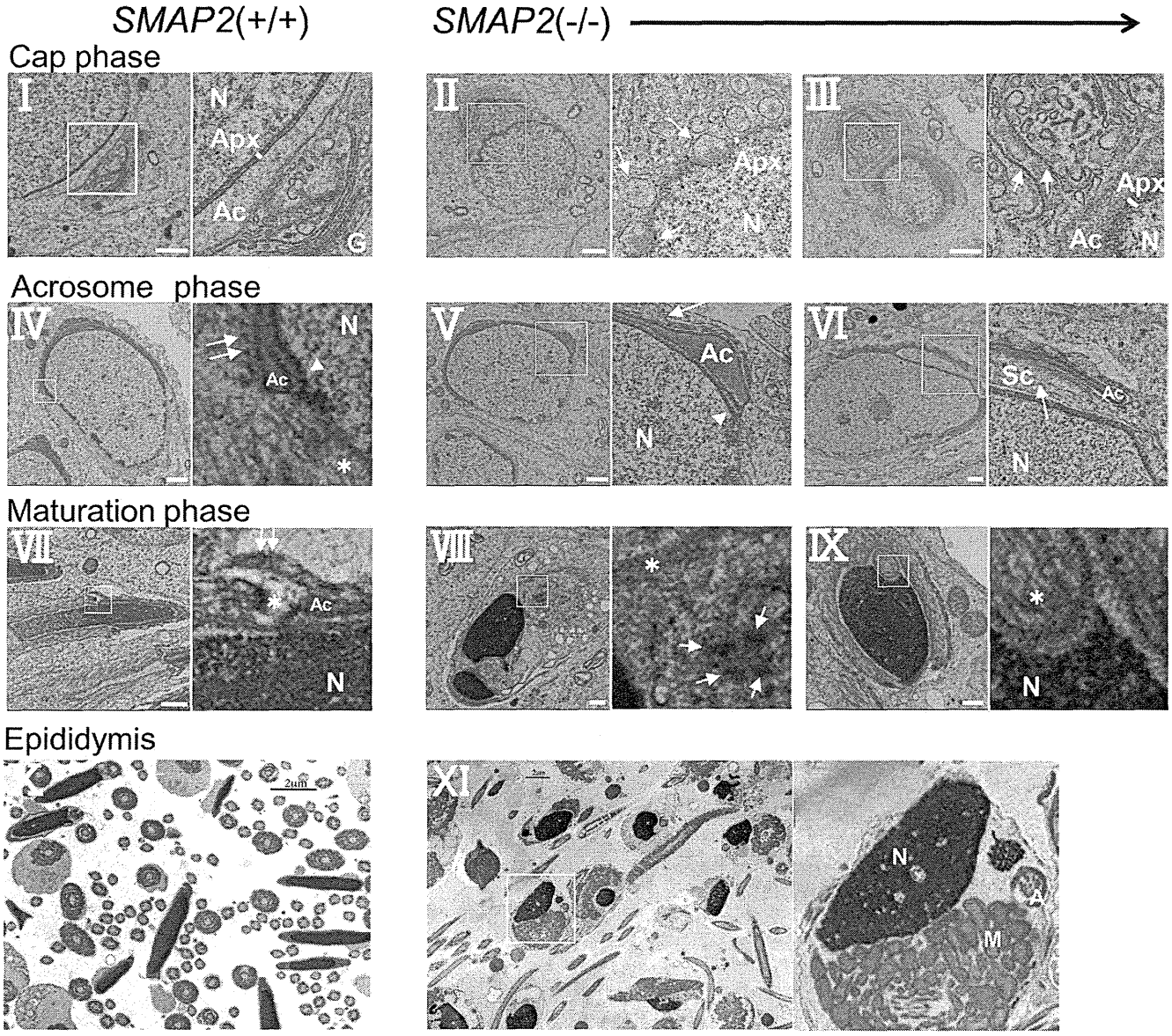

FIGURE 6: Electron microscopic observations of acrosome formation and subsequent events in wild-type and *SMAP2*-targeted germ cells. Cells at the cap, acrosome, and maturation phases of acrosome formation are shown. Sections of epididymides are also shown. See the text for the description of structural abnormalities. A, axoneme; Ac, acrosome; Apx, acroplaxome; G, Golgi apparatus; M, mitochondria; N, nucleus; Sc, Sertoli cell. Arrowheads in IV and V are marginal rings. Asterisks in IV and VII–IX are manchettes. Double white arrows in IV and VII are ectoplasmic specializations derived from Sertoli cells. White arrows indicate pseudoacrosomes (II), a disorganized TGN structure (III), interrupted ectoplasmic specializations (V), invagination of a Sertoli cell into the germ cell (VI), and fragmented acrosomes (VIII). Bars, 1 μm (I–IX), 2 μm (X, XI).

membrane, and eventually form a large organelle known as the acrosome (Abou-Haila and Tulsiani, 2000; Moreno and Alvarado, 2006). We reported previously that SMAP2 is located on the TGN and functions in vesicle transport from the TGN in tissue culture cells such as HeLa and Cos7 cells (Funaki *et al.*, 2011). These results suggested that SMAP2 might be directly involved in the budding of proacrosomal vesicles from the TGN in spermatogenesis. This hypothesis is supported by the following observations. 1) SMAP2 protein is detected in wild-type germ cells and in the pachytene spermatocyte to the round spermatid stages. Acrosomal proteins are actively synthesized at the pachytene stage (Anakwe and Gerton, 1990), and enormous amounts of proacrosomal vesicles are supplied from the TGN until the round spermatid stage. Thus the observed pattern of SMAP2 expression coincides with the period of acrosome formation. 2) In wild-type spermatogenic cells, SMAP2 is located exclusively on the TGN. 3) In *SMAP2*-deficient germ cells, the TGN tend to lose structural integrity, appearing as loose whorls, and the diameters of proacrosomal vesicles become significantly larger than in wild-type cells.

The primary alteration in spermiogenesis in *SMAP2*-deficient mice was the enlargement of the proacrosomal vesicles, suggesting that this change may ultimately cause the globozoospermic morphology. In other words, SMAP2 may function to standardize

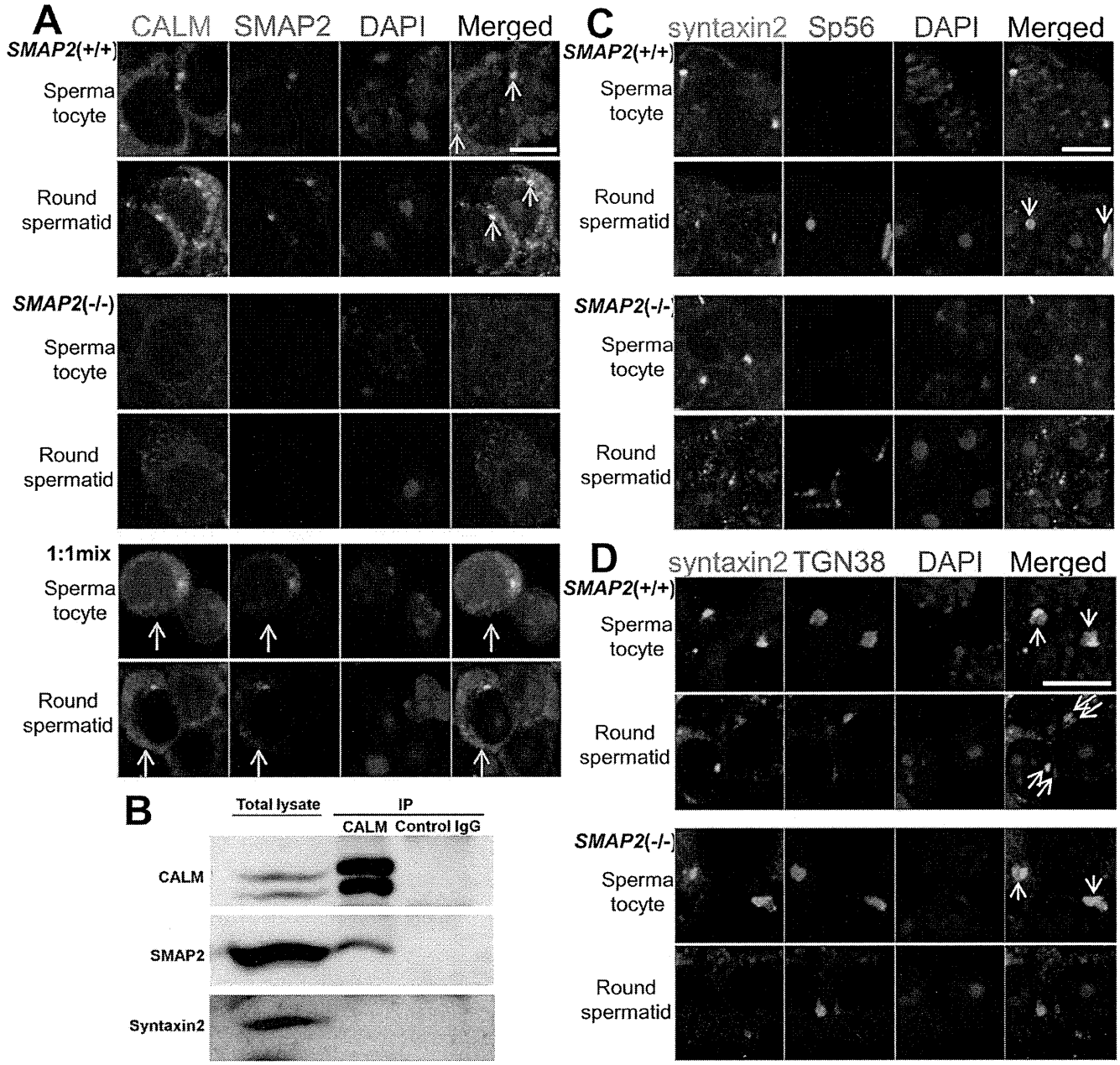

FIGURE 7: Subcellular localization of CALM and syntaxin2 as revealed by immunofluorescence staining. (A, C, D) *SMAP2*(+/+) and (–/–) germ cells were prepared as in Figure 3 and stained with anti-SMAP2, anti-CALM, anti-syntaxin2, anti-sp56, anti-TGN38, and DAPI, as indicated. The 1:1 mix is a mixed sample of *SMAP2*(+/+) and (–/–) cells. Pachytene spermatocytes and round spermatids are shown. Bar, 5 μm. (B) Immunoprecipitation of CALM. Lysates prepared from wild-type testes were immunoprecipitated with an anti-CALM antibody, and the precipitates were blotted with anti-CALM, anti-SMAP2, or anti-syntaxin2, as indicated.

the size of TGN-derived vesicles. Thus a principal issue is how SMAP2 might function to regulate vesicle size during vesicle formation. CALM and its homologue, AP180, control the size of clathrin-coated vesicles. When *CALM/AP180* is abolished, vesicles become enlarged (Zhang *et al.*, 1998; Nonet *et al.*, 1999; Meyerholz *et al.*, 2005), similar to the effects of *SMAP2* deficiency. We reported previously that SMAP2 binds to CALM directly (Natsume *et al.*, 2006). One possible scenario for *SMAP2* deficiency is that CALM is not recruited to the site of vesicle formation, thus causing the vesicle size to be unregulated. Consistent with this hypothesis, CALM is detected at the TGN in wild-type but not in *SMAP2*(–/–) cells.

In addition to the morphological abnormalities, *SMAP2*(–/–) proacrosomal vesicles may have other functional defects. Vesicle-associated membrane proteins (VAMPs) are components of the SNARE complex, and CALM can function to recruit some VAMPs to clathrin-coated vesicles through physical association with the VAMPs (Harel *et al.*, 2008; Koo *et al.*, 2011; Miller *et al.*, 2011). Therefore recruitment of SNARE complex components may be defective in *SMAP2*-deficient proacrosomal vesicles, since CALM was not